THE GEOTHERM, COMPOSITION AND STRUCTURE OF THE UPPER MANTLE AND TRANSITION ZONE

by

Wenbo Xu

A dissertation submitted in partial fulfillment
of the requirements for the degree of
Doctoral of Philosophy
(Geology)
in The University of Michigan
2008

Doctoral Committee:

Associate Professor Carolina R. Lithgow-Bertelloni, Co-Chair
Professor Larry Ruff, Co-Chair
Professor Charles R. Doering
Professor Lars P. Stixrude
Associate Professor Jeroen Ritsema

To my families and friends

Acknowledgements

First I would like to sincerely thank my advisor, associate professor Carolina Lithgow-Bertelloni. During my Ph.D study, she not only helped me making fast progress on research projects, but also taught me how to treat family and work. I even learned how to make a good plan for the future life from her. She is the best teacher in my life so far. I would also like to thank Professor Lars Stixrude and Associate Professor Jeroen Ritsema, who are collaborators of my research project. They guided me a lot by providing plenty good suggests.

In addition, we would like to thank geophysical group and department of geological sciences. They provide me the opportunity of Ph.D study in The University of Michigan, where I spent four years wonderful life and gained a lot. They also help me to touch and live in a totally different environment.

At last, I'd like to thank my families and friends. Because of their love and support, I successfully finished Ph.D study and could continuingly march to next step of my life.

Table of Contents

List of Figures

Figure

List of Tables

Table

List of Abbreviations

MM	Mechanical Mixture
EA	Equilibrium Assemblage
TNA	Tectonic North American Seismic model
WNA	Seismic model of Western North America
PREM	Preliminary referred Earth model
MORB	Mid-Ocean-Ridge-Basalt
DMM	depleted mid-ocean-ridge basalt model
plg	Plagioclase
sp	Spinel
opx	Orthopyroxene
c2c	High pressure clinopyroxene
gt	Garnet
cpv	Ca-perovskite
ol	Olivine
wa	Wadsleyite
ri	Ringwoodite
il	ilmenite
pv	Perovskite
ppv	Post-Perovskite
cf	Calcium-Ferrite
mw	Ferropericlase
qtz	Quarz
coes	Coesite
st	Stishovite
apbo	alpha lead oxide

Abstract

We use a self-consistent thermodynamic formalism to compute phase equilibria and physical properties and demonstrate that the seismological properties of a mantle comprised of (1) an equilibrium assemblage of pyrolitic composition and (2) a mechanical mixture of basalt and harzburgite with identical bulk composition are different. We calculate the shear wave velocity (V_S) for both compositional models in a mantle with basalt fractions that vary from 0% to 100% and along adiabats with potential temperatures ranging from 1000 to 2000K. For the mechanical mixture, V_S in the transition zone is higher. It increases more rapidly with depth, and it is virtually insensitive to basalt fraction, while for the equilibrium assemblage V_S decreases by 3.5% with increasing basalt fraction from 0% to 60%. The magnitude of the 520-km discontinuity depends strongly on temperature in both models, which may explain lateral variations in its seismic detection. Both compositional models feature "double-step" discontinuities in the range of 660-750 km due to the ringwoodite-perovskite transition and the gradual dissolution of garnet into perovskite between 665 km and ~725 km depth. The mechanical mixture is faster than most seismological models in the upper mantle, and slower in the lower mantle, suggesting an increase of basalt fraction with depth in the mantle. In addition, the geotherm of Western North America was inverted from two regional sheae wave velocity models. It strongly indicates a super-adiabatic geotherm in the low velocity zone and an asthenosphere fed by plumes rising from the core-mantle boundary. The inverted geotherm from both global and regional models suggests a sub-adiabatic temperature gradient in the transition zone, which can be explained by a slab accumulation of 30% by mass or volume in this region of the mantle. The latter is not only the consequence of phase transitions but of a large viscosity increase between upper and lower mantles.

Introduction

Earth's interior is inaccessible to direct observation. Our knowledge of its composition and structure largely derives from inferences based on the speed of seismic waves generated by earthquakes, analysis of meteoritic and volcanic samples, and comparison with laboratory measurements of seismic speeds. The goal of my thesis can be summarized in one sentence, reexamining the composition of the mantle from a dynamical perspective and its consequences for seismic structure. The central method of my dissertation is the application of a new self-consistent thermodynamic model of the mantle, with which I explore forward models of physical properties for different mantle compositions and then apply in an inverse sense to explore the temperature structure of the upper mantle and transition zone.

The pattern of mantle convection has been the subject of much debate and study and cartoons like those in Figure 0.1, which range from completely segregated upper and lower mantles to whole mantle convection have been largely inspired by trace element geochemistry. Indeed geochemistry gives us the colors, but cannot tell us the shape or even the exact location (as illustrated by the cartoons) of these reservoirs. The different regions are represented by one color, say the blue of the oceanic lithosphere or the green of its basaltic crust and imply homogeneity. But what is really the case?

Dynamically, as shown in the mantle convection calculations of Xie and Tackley (2004) in Figure 0.2, we don't expect homogeneous reservoirs. Indeed, what we see here are not homogeneous reservoirs but rather as the oceanic lithosphere subducts, separation of different compositions, which as they mix and stretch, lead to a mechanical mixture of basalt and harzburgite (the partial melting product and its depleted residuum) Let's examine what happens at the ridge, the trench and the mantle in more detail (Figure 1.1). Beneath mid-ocean ridges, an upwelling mantle source is partially molten to form Mid-ocean Ridge Basalt (MORB). The depleted residual (harzburgite) is left behind, and forms the great majority of the oceanic lithosphere beneath the basaltic crust.As the oceanic lithosphere ages and cools part of the unmelted MORB source also forms the oceanic lithosphere. At the trench, the slab, chemically layered, subducts, introducing continuous chemical and thermal heterogeneity into the mantle.With depth the mantle undergoes pressure-induced crystal structure transformations to closer-packed structures, which densify the material. However, these are both composition and temperature dependent. Because the oceanic lithosphere is cold and chemically layered we expect different phase transitions to occur with respect to normal mantle and with respect to each layer. Indeed, basalt undergoes one of the first major transitions as it transforms to eclogite, and becomes considerably denser than the harzburgite underlying it. The end result is separation of the basaltic crust from the oceanic lithosphere upon subduction. Although the exact process of separation is not clear and there is considerable debate over how much the slab deforms and whether there is full slab penetration into the lower mantle, the key point is that partial melting products, basalt and harzburgite, do re-cycle back to mantle and likely separate. If this is the case, then what is the fate of the separated

basalt and harzburgite (Figure 1.1)? What emerges from the dynamical simulations (Figure 0.2) is a mantle that is mechanically mixed and progressively enriched in basalt. This material stretches and folds, but not enough for the very low values of chemical diffusivity in the mantle (10^{-14}-10^{-16} m^2 s^{-1}) to ensure chemical reequilibration into a homogeneous material. While this picture of the mantle has been evident for some time its ultimate consequences and implications for mantle composition and seismic structure have not been examined. This picture suggests two things 1) the potential for mantle composition to be defined in terms of rocks that are not equilibrated and 2) that we have a natural metric, that arises from a dynamical genetic process, to study the effects of composition on seismic structure: the basalt fraction.

The conventional view is that mantle is pyrolitic (Bass, 1995; Chen, et al., 1991; Frey, et al., 1978; McKenzie and Bickle, 1988; Ringwood, 1969). This view suggests that the chemically layered oceanic lithosphere is re-homogenized into a chemically reequilibrated pyrolitic mantle. Although it guarantees that MORB source is replenished continuously, this model appears to violate dynamical models of the Earth's mantle taking into account the low chemical diffusivity in the solid state at mantle temperatures and pressures. In fact dynamical models favor a heterogeneous mantle made of a mechanical mixture of basalt and its depleted residual harzburgite (Nakagawa and Buffett, 2005; van Keken et al., 2002; Xie and Tackley, 2004), in which basalt enrichment increases with depth. It therefore seems implausible to re-equilibrate subducted basalt and harzburgite into pyrolite, except perhaps near the ridge in the presence of partial melt where chemical diffusion rates would increase by orders of

magnitude. These two models would strongly signal different chemical, geothermal, and dynamical evolutionary paths for Earth's mantle.

I address this conundrum by examining the variation in expected physical (seismic) properties of these two end members: homogeneous pyrolite, here called equilibrium assemblage (EA), on one hand (Xu et al., 2008), and a mechanical mixture of basalt and harzburgite, (MM), on the other hand and comparing them to seismic models. In fact, can we distinguish between these two end members? The premise of this thesis is yes. Because EA and MM have different mineral proportions for an identical bulk composition, we expect very different phase diagrams (i.e. existence of particular phase and proportion of each phase for a given set of conditions such as composition, temperature and pressure) as a function of depth in the mantle. Hence, we expect different physical property profiles and in consequence seismic wave velocity structure.

To investigate these questions we use self-consistent thermodynamic petrologic model of the mantle to compute physical properties and phase equilibria developed by Stixrude and Lithgow-Bertelloni (2005a;b), which captures complete information of assemblage at given temperature and pressure by taking Legendre transformation and derivatives of the Gibbs free energy. The methods are described fully in the above references and concisely in Chapter 1. I use a simplified compositional model with six oxide components: CaO, FeO, MgO, SiO_2, Al_2O_3, Na_2O, and 45 mineral species. Armed with this model I use the whole rock compositions of Workman and Hart (2005) for Depleted Mid-Ocean Ridge-Basalt Mantle (DMM) to represent pyrolite and for MORB to represent basalt. The composition of harzburgite is modified based on the most recent depletion models (Baker and Beckett, 1999).

In Chapter 1, I explore the influence of composition in terms of basalt depletion and enrichment, and a large range of potential temperatures for the upper 1000 km of the mantle. I show that not only are EA and MM distinct in their seismic properties, but that MM is a better fit to spherically averaged seismic models of the mantle. Indeed I find that using MM, because of its insensitivity to composition between 400-660 km depth (the transition zone) I can construct a unique thermometer for this region of the mantle, a topic I return to in Chapter 3. In Chapter 2 I move to a much shallower part of the mantle and study the seismic structure beneath the Western USA. In this part I examine the effects of dissipation of seismic energy and invert for the temperature profile that best-fits two distinct shear wave models of Western North America (Grand and Helmberger, 1984; Merret et al., 2007). I take into account the effects of temperature and grain size on dissipation and find that the low-velocity zone (LVZ, a distinct seismic feature under young and old oceans coincident with the so-called asthenosphere) is superadiabatic (40-80 K hotter than the normal mantle adiabat of 1600 K) and it quickly cools below adiabatic values as it approaches 400 km depth. This result is robust with respect to inversion methods, seismic velocity and attenuation models. I conclude that the asthenosphere is likely a plumeyard, a region of the mantle hotter because of the junction of the conductive cooling process of the thermal boundary layer with the adiabatic convective process of the interior, enhanced by temperature anomalies from narrow plume-like upwellings that die here as they warm the lithosphere above. This is in agreement with previous studies by Morgan and Morgan (1999).

Below the LVZ towards the bottom of the upper mantle at 400 km depth, lies the transition zone (410-660 km depth). This is a region of the mantle where there has been

considerable debate as to its composition and structure (Anderson,1986, Duffy and Anderson, 1989. Ita and Stixrude, 1992, 1993). It is bracketed by the two largest and likely most important pressure-induced phase transformations in the main mineral component of the mantle: olivine transforms from its ambient structure to a closer-packed phase called wadsleyite at 410 km depth, to ringwoodite at 520 km depth and finally to the most abundant mineral in the Earth, perovskite plus ferropericlase at 660 km depth. The lack of agreement between seismic models, the detailed structure and amplitude of seismic discontinuities, and proposed mantle compositions and phase transformations, have suggested that the transition zone may be a barrier to mass flux between upper and lower mantle. Indeed, even if not a complete barrier it may well inhibit undisturbed penetration of slabs into the lower mantle. Understanding the temperature, chemistry, mineral and seismic structure of this region is key to answering the question: What is the fate of slabs? Numerical models of mantle convection with phase transitions (e.g. Christensen, 1995; Honda et al., 1993; Machetel and Weber 1991; Solheim and Peltier 1994; Tackley et al., 1993; Weistein 1993;) imply slab accumulation in the transition zone, which may the avalanche into the lower mantle when a critical amount of slab is attained. Consequently, we should expect on average that the transition zone will be sub-adiabatic with respect to the normal mantle geotherm, which we take to represent the mid-ocean ridge. In Chapter 3, taking advantage of the detail knowledge of how composition and temperature affect the two proposed compositional end-members, I reprise the question of the temperature structure of the transition zone. As in Chapter 2, I invert for the temperature that best-fits two different shear-wave velocity profiles for the mantle: PREM-a global spherically averaged model and TNA, a regional model for

Western North America. I examine the effects of basalt enrichment on the inverted geotherms and the deviations implied by the inverted geotherm for other physical properties, including compressional velocity and density. The results robustly show that the transition zone is indeed subadiabatic by 150-250 K, implying a slab volume of as much as approximately 25%-35% in this region.

This detailed examination of mantle physical properties leads us to dramatically reassess our understanding of mantle composition and temperature structure. First, I conclude that the mantle is best represented as a mechanical mixture of basalt and harzburgite, with a gradual enrichment in basalt, and not a homogeneous or layered system. Second, that the asthenosphere is hotter than the adiabat because it contains the remnant of mantle plumes. Third, that the transition zone is sub-adiabatic by 150-250 K because of slab accumulation in the transition zone, which is due to 30% slab accumulation in the transition zone. Indeed we should not consider the 1600 K ridge adiabat the average mantle, but rather a normal mantle, where the average is substantially cooled by subduction, instead. These results should challenge many conventional views regarding the dynamical and chemical evolution of the planet as well as commonly used comparisons between seismic wave velocity and density.

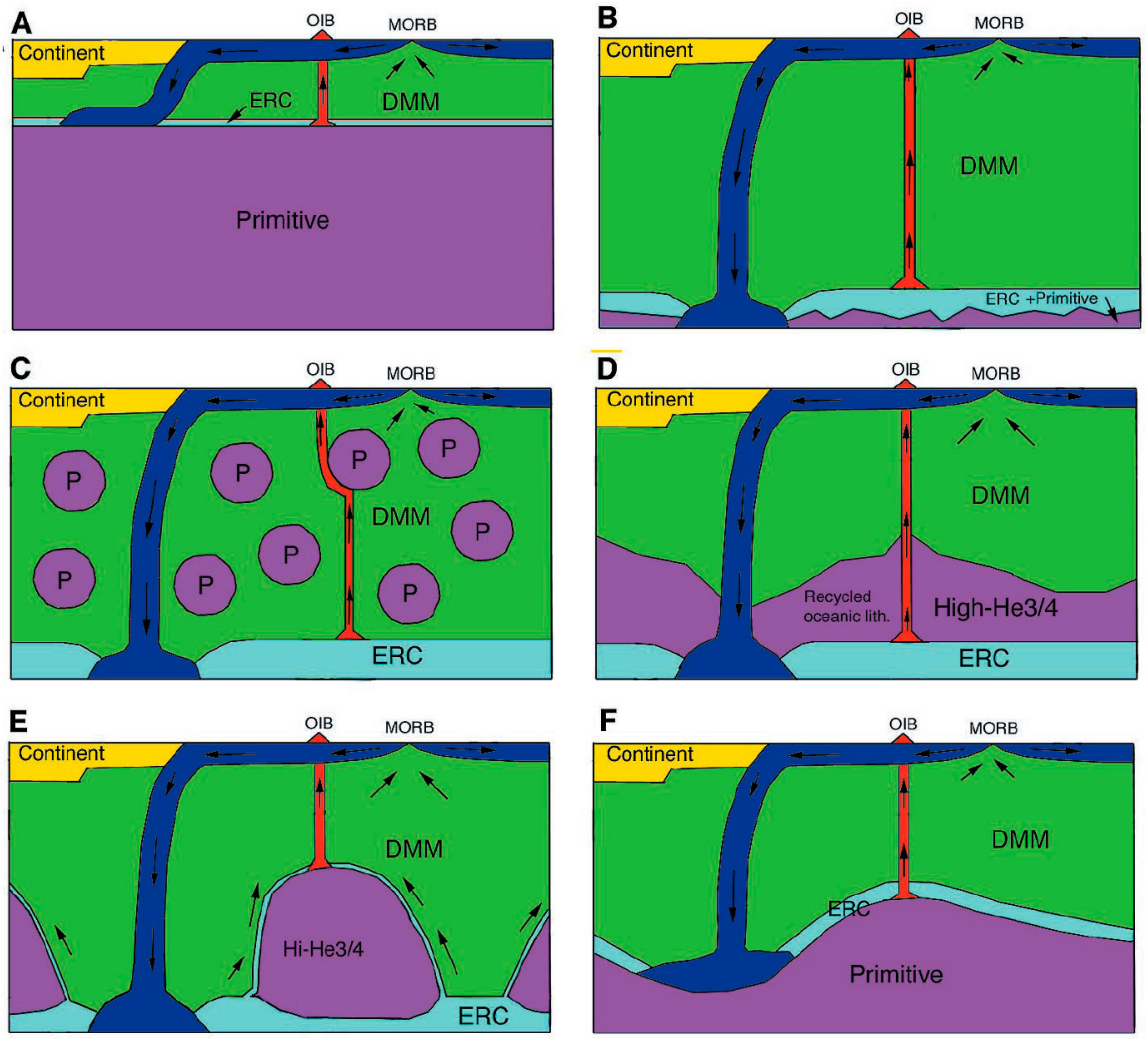

Figure 0.1, Some possible locations of mantle reservoirs and relationship to mantle dynamics. Convective features blue, oceanis plates/slabs, hot plutme. Geochemical reservoirs: dark green, DMM; purple, high $^{3}He/^{4}He$("primitive"); light green, enriched recycled crust(ERC). (A) Typical geochemical model layered at 660 km depth. (B) Typical geodynamical model: homogenous except for some mixture of ERC and primitive material at the base. (C) Primitive blob model with added ERC layer. (D) Complete recyling model. (E) Primitive piles model. (F) Deep primitive layer. From Tackley (2000)

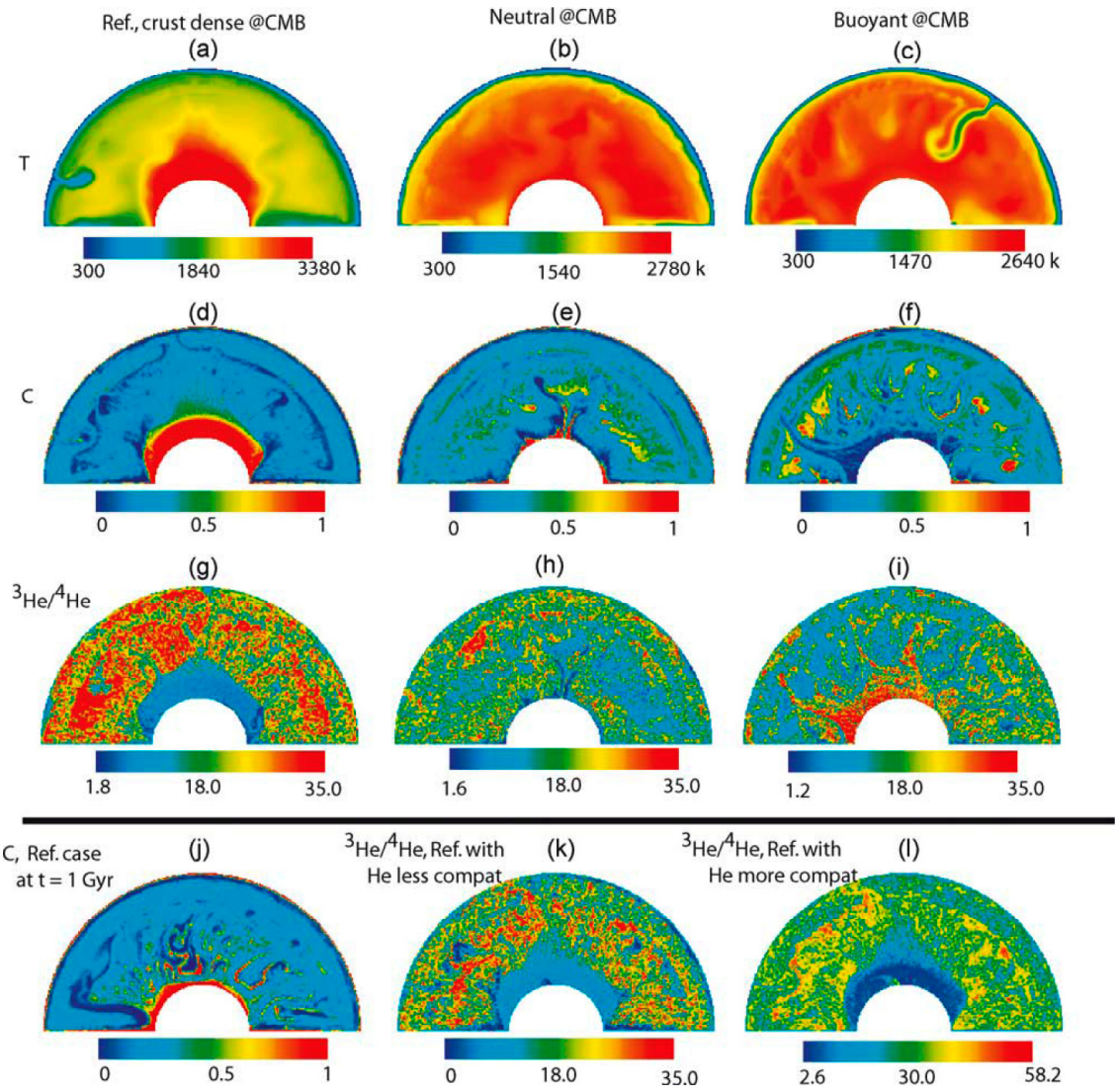

Figure 0.2 Earth internal structure at present day (after 3.6 Gyr except (j) of reference case (left column), case with neutral buoyant crust at CMB (middle column, except k), case with byoyant crust at CMB (right column, except l), case with helium less compatible than uranium(k), case with helium more compatible than uranium(l). (a-c) Temerature field, from cold (blue) to hot (red). (d-f) composition, ranging from basalt/ecologite (red) to harzburgite(blue). (g-l) except (j) $^3He/^4He$ (relative to atmospheric value) ranging from min (blue) to max(red). (j) Composition field of reference case at t = 1.0 Gyr. From Xie and Tackley (2004).

References:

Anderson, D.L., Bass, J.D., 1986. Transition Region Of The Earth Upper Mantle. Nature 320, 321-328.

Baker, M.B., Beckett, J.R., 1999. The origin of abyssal peridotites: a reinterpretation of constraints based on primary bulk compositions. Earth Planet. Sci. Lett. 171, 49-61.

Bass, J. D., 1995. Elasticity of minerals, glasses, and melts, in Mineral Physics and Crystallography, in: Ahrens, T.J., A handbook of physical constants, AGU, Washington, D.C. pp. 465-63.

Chen, C.Y., Frey, F.A., Garcia, M.O., et al. 1991. The tholeiite to alkalic basalt transition at Haleakala Volcano, Maui, Hawaii. Contributions to Mineralogy and Petrology 106, 183-200.

Christensen, U., 1995. Effects of phase transitions on mantle convection. Annu. Rev. Earth plant. Sci. 23, 65-87

Duffy,T.S. and Anderson, D.L., 1989. Seismic velocities in mantle minerals and the mineralogy of the upper mantle. J.Geophys. Res. 94, 1895-1912

Frey, F.A., Green, D.H., Roy, S.D., 1978. Integrated models of basalt petrogenesis: A study of Quartz Tholeiites to Olivine melilitites from south eastern Australia utilizing geochemical and experimental petrological data. J. Petrology 19, 463-513.

Grand, S.P., Helmberger, D.V., 1984. Upper Mantle shear Structure of North America. Geophys. J.R. astr. Soc. 76, 399-348

Ita, J. J., and Stixrude, L., 1992. Petrology, elasticity and composition of the transition zone. J. Geophys. Res. 97, 6849-6866.

Ita, J. J. and Stixrude, L., Density and elasticity of model upper mantle compositions and their implications for whole mantle structure, in Evolution of the Earth and Planets, Geophysical Monograph 74, edited by E. Takahashi, R. Jeanloz and D. Rubie, International Union of Geodesy and Geophysics and American Geophysical Union, Washington, D. C., pp. 111-130, 1993

Machetel P, and Weber P. 1991. Intermittent layered convection in a model with an endothermic phase change at 670 km. Nature 350:55-57

Mckenzie, D., and Bickle, M.J., 1988. The volume and composition of melt generated by extension of the lithosphere. J. Petrology 29, 625-679.

Merrer, S., Cara, M., Rivera, L., et al., 2007. Upper mantle structure beneath continents: New constraints from multi-mode Rayleigh wave data in western North American and south Africa. Geo. Res. Lett., Vol. 34, L06309, doi:10.1029/2006GL028939.

Morgan, J.P., and Morgan, W. J., 1999. Two-stage melting and the geochemical evolution of the mantle: a recipe for mantle plume-pudding. Earth Plant. Sci. Lett., 170, 215-239

Nakagawa, T., and Buffett, B.A., 2005. Mass transport mechanisms between the upper and lower mantle in numerical simulations of thermo-chemical mantle convection with multi-component phase changes. Earth Planet. Sci. Lett. 230, 11-27.

Ringwood, A. E., 1969. Composition and evolution of the upper mantle, in: Hart, P.J., The Earth's Crust and upper mantle: structure, dynamic process, and their relations to deep-seated geological phenomena. Geophys. Mongr. Ser. 13, Washington, D. C., 1-17.

Stixrude, L., Lithgow-Bertelloni, C., 2005a. Mineralogy and elasticity of oceanic upper mantle: Origin of the low velocity zone. J Geophys. Res. 110, B03204, doi:10.1029/2004JB002965

Stixrude, L., Lithgow-Bertelloni, C., 2005b. Thermodynamics of mantle minerals I: Physical properties. Geophys. J. Int. 162, 610-632.

Solheim LP, and Peltier WR. 1994a. Avalanche effects in phase transition modulated thermal convection: a model for the Earth's mantle. J. Geophys. Res. 99:6997-7018

Tackley PJ, Stevenson D J, Glatzmaier GA, et al. 1993. Effects of an endothermic phase transition at 670 km depth in a spherical model of convection in the Earth's mantle. Nature 361:699-704

Workman, R.K., and Hart, S. R., 2005. Major and trace element composition of the depleted MORB mantle (DMM). Earth Planet. Sci. Lett. 231, 53-72.

Xie, S., and Tackley, P., 2004. Evolution of U-Pb and Sm-Nd systems in numerical models of mantle convection and plate tectonics. J. Geophys. Res. 109, 10.1029/2004JB003176.

Xu, W., Lithgow-Bertelloni, C., Stixrude, L., et al., 2008. The Effect of Bulk Composition and Temperature on Mantle Seismic Structure. Earth Plant. Sci Lett., Submitted

van Keken, P.E., Hauri, E., and Ballentine, C., 2002 Mantle mixing: the generation, preservation, and destruction of mantle heterogeneity, Ann. Rev. Earth Planet. Sci., 30, 493, 2002

Weinstein SA. 1993. Catastrophic overturn of the Earth's mantle driven by multiple phase changes and internal heat generation. Geophys. Res. Lett. 20:101-4

Honda S., Yuen DA, Balachandar S., et al., 1993. Three-dimensionalinstabilities of mantle convection with multiple phase transitions. Science 259:1308-1

Chapter I
The Effect of Bulk Composition and Temperature on Mantle Seismic Structure

1.1 Introduction

At mid-ocean ridges, partial melting generates a basaltic crust and leaves behind its depleted complement, harzburgite. The oceanic lithosphere thus formed is physically and chemically layered, and when the lithosphere subducts back into the mantle, the basalt to eclogite transition causes basalt and harzburgite to separate (Figure 1.1). Do basalt and harzburgite re-equilibrate chemically as pyrolite? If they do, over what time scales? If not, should we consider the mantle as a non-equilibrated mechanical mixture of basalt and harzburgite?

Experiments have shown that a homogeneous pyrolite source region can explain the observed composition of mid-ocean ridge basalt (Chen, et al., 1991; Frey, et al., 1978; McKenzie and Bickle, 1988) and the seismic velocity profile of upper mantle and transition zone to first order (Irifune, 1993; Ita and Stixrude, 1992; Ringwood, 1979; Weidner, 1985). Indeed, nearly all mineralogical models, upon which comparisons to seismology are based, view the mantle as homogeneous and pyrolitic (Bass, 1995; Francis, 1987; Ringwood, 1966,1969) or chemically stratified with homogeneous and equilibrated compositions in each layer (e.g. Anderson and Bass, 1986; Mattern et al., 2005). However, the assumption of major element chemical equilibrium appears at odds with the low chemical diffusivity for mantle materials (10^{-14}-10^{-16} m^2 s^{-1}) in the solid-state

(Allégre and Turcotte, 1986; Farber et al., 1994; Yamazaki, et al., 2000), if we may ignore the effects of fluids and partial melting on a global scale.

Mechanically mixed mantle models have been considered as well. Allègre and Turcotte (1986) suggested a marble cake structure for the mantle in which subducted oceanic lithosphere is deformed into pervasive, narrow pyroxenite veins. Mantle convection simulations suggest a heterogeneous mantle made of a mechanical mixture of basalt and harzburgite, in which pools of basalt may accumulate at the bottom (Brandenburg and Van Keken, 2007; Christensen and Hofmann, 1994; Davies, 2006; Nakagawa and Buffett, 2005; Xie and Tackley, 2004). A stirring time of the mantle between 250 and 750 Myr (Kellogg et al., 2002) limits the amount of stretching and folding of subducted heterogeneity that can occur in the mantle. It seems thus implausible to re-equilibrate subducted basalt and harzburgite, which have significantly different physical properties, into pyrolite.

In this paper, we explore the effects of major element disequilibrium on seismological properties of the mantle. We demonstrate that even with identical bulk compositions, an equilibrium assemblage along the basalt-harzburgite join and a mechanical mixture of basalt and harzburgite have different phase equilibria and therefore different seismic velocities. We explore the influence of potential temperature and bulk composition, using the relative proportions of basalt and harzburgite (the basalt fraction) as a compositional metric. We consider two end-member models for combining basalt and harzburgite fractions in the mantle: (1) the Equilibrium Assemblage (EA) with

perfect re-equilibration and (2) the Mechanical Mixture (MM) with perfect disequilibrium between the two fractions.

We compute the seismic velocities of EA and MM following the self-consistent thermodynamic model developed by Stixrude and Lithgow-Bertelloni (2005a, 2005b). We focus in particular on shear wave velocity (V_S), which is most sensitive to our mineralogical parameters and which is best constrained by a combination of travel-time, surface wave and normal mode data.

1.2 Methodology

1.2.1 Compositional Model

The phase assemblages for EA

$$\phi\left[f\mathbf{X_B} + (1-f)\mathbf{X_H}\right] \tag{1.1}$$

and MM

$$f\phi\left[\mathbf{X_B}\right] + (1-f)\phi\left[\mathbf{X_H}\right] \tag{1.2}$$

with identical bulk compositions are significantly different. There $\backslash$ is the vector of phase proportions, **X** is the vector defining the bulk composition, subscripts B and H refer to basalt and harzburgite respectively, and f is the basalt fraction. In this study, we explore a variety of bulk compositions represented by the basalt fraction f, in the equilibrium (Eq. 1.1) and disequilibrium (Eq. 1.2) limits. We focus on a simplified model of mantle composition with five components: CaO, FeO, Al_2O_3, MgO, SiO_2, 14 phases, and 31 mantle species (Stixrude and Lithgow-Bertelloni, 2005b). We take as our reference estimate of the bulk composition of the mantle the Depleted Mid-Ocean-Ridge-Basalt Mantle (DMM) of Workman and Hart (2005). We approximate the composition of basalt,

$\mathbf{X_B}$ as the MORB model of Workman and Hart (2005) and the composition of harzburgite, $\mathbf{X_H}$ as the most depleted composition of abyssal peridotites from Baker and Beckett (1999) (Table 1). We slightly modify the harzburgite composition, and determine the basalt fraction f_P that produces the DMM composition, $\mathbf{X_P}$ such that

$$\mathbf{X_P} = f_P \mathbf{X_B} + (1 - f_P)\mathbf{X_H^*} \tag{1.3}$$

is exactly satisfied and the quantity

$$\varepsilon\left(f_P, \mathbf{X_H^*}\right) = \sum_{j}^{phases} \left[\phi_j\left(\mathbf{X_H}\right) - \phi_j\left(\mathbf{X_H^*}\right)\right]^2 \tag{1.4}$$

is minimized at 0 GPa, and 1600 K, where $\mathbf{X_H^*}$ is our modified harzburgite composition.

We find from this analysis that the basalt fraction of the mantle f_P=18%. A similar value is found from a simple analysis of tectonic rates. Assuming that: 1) the oceanic crust is 7 km thick, 2) the Cenozoic mean value of the rate of subduction of 3.35 km^2/yr (Xu et al., 2006) is representative of the last 4.6 Ga of Earth's history, 3) the entire mantle has been differentiated at least once, and 4) re-equilibration is inefficient, we find a basalt fraction of 12%. A similar analysis (Morgan and Morgan, 1999) found f_P~20 % by considering greater tectonic rates in the past. MORB compositions also suggest a significant fraction of recycled oceanic crust in the MORB source (Hirschmann and Stolper, 1996). Petrological estimates based on olivine phenocryst compositions suggest f_P=2-20% (Sobolev et al., 2007).

1.2.2 Thermodynamic Method

We apply a newly developed thermodynamic, petrologic formalism (Stixrude and Lithgow-Bertelloni, 2005a, 2005b), which enables self-consistent computations of

physical properties, phase equilibria, and mantle isentropes. This model uses the concepts of fundamental thermodynamic relations (Callen, 1960) and Legendre transformations to capture complete information of all equilibrium states in a single functional form. Generalization of the usual isotropic thermodynamics to conditions of anisotropic stress and strain permit self-consistent computation of the full elastic constant tensor, including the bulk and shear moduli, and therefore the longitudinal and shear seismic wave velocities, V_P and V_S, respectively.

Our calculations consist of three steps. We compute: (1) the equilibrium phase assemblage: the amounts and compositions of coexisting phases by minimizing the Gibbs free energy with respect to the amounts of species at fixed temperature, pressure, and bulk composition, (2) the physical properties of individual phases in the equilibrium compositions via stress and temperature derivatives of the Gibbs free energy, and (3) the elastic properties of the assemblage as the Voigt-Reuss-Hill average (Watt et al., 1976). For MM, steps (1-3) are carried out for basalt and harzburgite compositions separately and; in a fourth step, the elastic properties of the aggregate are determined via a Voigt-Reuss-Hill average of the components (basalt and harzburgite) of the mixture. To focus on the influence of bulk composition and major element disequilibrium, we do not include the effects of attenuation, i.e. velocities are in the infinite frequency, elastic limit.

1.3 Results

1.3.1 Influence of disequilibrium

Models EA and MM yield different phase equilibria for the same bulk composition (Figure 1.2). The amount of olivine at low pressure in EA is ~56%, while it

is 65% in MM. Stishovite appears in MM, but is absent from EA. The garnet-pyroxene fraction is less in MM. The influence of disequilibrium can be understood by considering the variation of phase proportions with f at 300 km depth (Figure 1.2, bottom). In the case of MM, stishovite is present at all non-zero values of f because it is stable in the basalt fraction, while in EA stishovite is not stabilized until f exceeds 70 %. The differences between MM and EA can be cast schematically as the reaction

$$MgSiO_3\ (EA) = Mg_2SiO_4\ (Hz) + SiO_2\ (Bs) \qquad (1.5)$$

where the right hand side represents the harzburgite (Hz) and basalt (Bs) fractions of the mechanical mixture with more olivine and free silica and less pyroxene than in the equilibrium assemblage.

Since the phase equilibria differ, the seismic velocity of EA and MM are not the same (Figures 1.2-4). Tables of computed values of V_P, V_S, and density for EA and MM as a function of basalt fraction and temperature may be found in the supplementary material. Both the compressional (~0.08 km/s) and the shear wave velocity (~0.06 km/s) of MM are higher than that of EA in most of the upper mantle and transition zone due to the lower proportion of low-velocity phases, such as clinopyroxene (cpx) and the presence of stishovite, a high-velocity mantle phase. The velocity profiles of MM have a greater radial gradient than EA in the deeper transition zone because of the relatively high proportions of wadsleyite, ringwoodite, Ca-perovskite, and akimotoite, and the relatively low proportion of garnet.

The discontinuity structures in the EA and MM models differ as well. The EA velocity structure has a discontinuity at a depth similar to the Hales discontinuity (60 km), associated with the transition from spinel to garnet. This discontinuity is absent in

MM. The MM shows a large increase in velocity at the basalt to eclogite transition near 100 km depth. A discontinuity near X discontinuity at 280 km depth (Revenaugh and Jordan, 1991; Woodland, 1998) is present in both models presumably due to the opx-C2/c transition. Since our models do not include silica phases other than stishovite we cannot rule out that the X discontinuity involves a transition from coesite to stishovite (Williams and Revenaugh, 2005).

The depth and velocity contrast of the 410 and 660 km discontinuities are similar in EA and MM, although the latter has somewhat greater velocity contrasts at both discontinuities, due to the greater olivine fraction. In agreement with recent observations of reflected and converted phases (Lawrence and Shearer, 2006) our results show a 660 km discontinuity nearly 3 times narrower than the 410 km discontinuity. The high velocity gradient immediately below 660 km in EA is due to the gradual transformation of garnet to perovskite. This structure is absent in MM, which has a lesser proportion of garnet at this depth. The 520 km discontinuity is more prominent in MM due to the larger proportion of wadsleyite and ringwoodite, as compared with EA. MM shows an additional velocity discontinuity near 750 km that is due to the garnet to perovskite transition in the basalt fraction. We believe this feature to be robust, although we note that below 660 km we find no calcium-ferrite phase, as seen experimentally. We attribute this discrepancy to the neglect of the sodium component in our studies, which will stabilize the calcium-ferrite phase (Hirose et al., 2005).

1.3.2 Influence of bulk composition

In EA, V_S increases with increasing basalt fraction except in the transition zone, at depths shallower than 80 km, and between 660-750 km (Figure 1.5). These variations can readily be understood on the basis of the phase equilibria: as basalt fraction increases, olivine (a relatively low-velocity phase) proportion decreases, while the garnet (a relatively high-velocity phase) proportion increases. In the transition zone, olivine transforms into wadsleyite and ringwoodite, both of which are faster than garnet. Especially when the basalt fraction exceeds 70%, not only is stishovite (a fast phase) stabilized but its proportion grows. So V_S in the transition zone may decrease (f <70%) or increase (f >70%) as function of basalt fraction. The velocity varies non-linearly with basalt fraction, so that the compositional derivative dV_S/df, where f is basalt fraction, is a strong function of bulk composition. The depth and thickness of discontinuities vary with composition: In EA, the 410 km discontinuity is slightly shallower (~10 km) and substantially sharper (17 vs. 11 km, respectively) when basalt fraction f is increased from 0 to 0.4. The shallower depth of the transition can be explained by the increasing iron content with increasing f (from X_{Fe}=Fe/(Fe+Mg)=9.6 % to 13.5%), which tends to stabilize wadsleyite to lower pressures at the expense of olivine. The increase in Fe, combined with the influence of partitioning among transforming and non-transforming phases (Stixrude, 1997) accounts for the change in sharpness. The transition near 410 km depth disappears completely for f>80 % as olivine is no longer stable (Figure 1.2). The velocity gradient directly below the 410 km discontinuity is significantly influenced by the phase change of cpx to garnet. The high velocity gradient zone immediately below the 660 km discontinuity is due to the gradual transformation of garnet to perovskite, and its width increases with increasing basalt (garnet) fraction: it is 80 km wide (665-744 km

depth) for f=0.4, and nearly absent (663-668 km depth) when f=0. When f> 84%, the gradual transformation of garnet to perovskite disappears and a sharp transition of garnet to perovskite+Al-rich akimotoite appears at 745 km.

The results are very different for MM (Figure 1.5). V_S increases with basalt fraction throughout the entire mantle, except for depths shallower than 100 km, and in the interval 660-740 km depth. This is due to the presence and increasing proportion of stishovite with increasing basalt content; and to a lesser extent to the decreasing proportion of olivine and the increasing proportion of garnet. In the transition zone, the velocity is nearly independent of basalt fraction ($dV_S/df \sim 2 \cdot 10^{-2}$km s^{-1}). Between 660 km and 740 km depth, the velocity decreases with basalt fraction because the garnet to perovskite transition occurs at a greater depth in basalt than it does in harzburgite. The depths and widths of the major discontinuities near 410 km and 660 km discontinuities are unaffected by variations in f since these are due entirely to transformations occurring in the harzburgite fraction. The 520 km discontinuity is substantially smaller than the 410 or 660-km discontinuities due to the relatively small impedance contrast between wadsleyite and ringwoodite. In MM there are two sharp features due to the ringwoodite=perovskite+ferropericlase transition in the harzburgite component (660 km), and the garnet=akimotoite+perovskite transition in the basalt component (745 km).

1.3.3 Influence of Temperature

Temperature influences the velocity of the aggregate via its influence on the elasticity of constituent phases and the phase equilibria (Anderson, 1987; Stixrude and Lithgow-Bertelloni, 2007) (Figure 1.6). For example, in regions that are not strongly

influenced by phase transformations, the average derivative of velocity with respect to temperature dV_S/dT is similar in EA and MM (-3.4×10^{-4} km s^{-1} K^{-1} and -3.0×10^{-4} km s^{-1} K^{-1} at 200 km and 800 km, respectively). Temperature modifies the depths of the olivine to wadsleyite and ringwoodite to perovskite and ferropericlase transitions. These transitions occur at, respectively, deeper and shallower depths with increasing temperature, reflecting the opposite signs of the effective Clapeyron slopes. In the vicinity of phase transformations, the temperature derivatives vary rapidly and are very different in MM and EA.

The range of temperature between 1000 K and 2000 K, both of which are potential temperature for adiabat, explored reveals three significant aspects of the phase equilibria as they influence the velocity structure. The First aspect is the appearance of a double 660 km discontinuity at the lowest temperatures explored: the velocity increase at this discontinuity occurs in two sub-equal steps, separated in depth by approximately 10 km. These two steps are due to the following sequence of transformations: ringwoodite=akimotoite+ferropericlase, akimotoite=perovskite, which occur only at low temperature where akimotoite is favored at the expense of garnet, and which replaces the high temperature sequence: akimotoite=perovskite, ringwoodite=perovskite+ferropericl-ase. In addition to these sharp transitions a high gradient zone is present immediately beneath the 660 km discontinuity due to the garnet to perovskite transition, which is present in EA at all but the coldest temperatures, and becomes more prominent in MM at high temperatures. The structure of the 660 km "discontinuity" may be quite complex and the structure that we find may be consistent with seismological observations of a "doubled" 660 km discontinuity (Deuss et al., 2006; Lawrence and Shearer, 2006;

Simmons and Gurrola, 2000). The Second aspect is transformations of garnet to Ca-perovksite, which occurs over a broad range of pressures at all temperatures, and garnet to akimotoite, which occurs at potential temperatures ≤1600 K. These two transformations produce enhanced radial velocity gradients at depths greater than 520 km that are most apparent at the lowest potential temperatures in EA. We note in this context that the pressure range over which the garnet to Ca-perovskite transition occurs in our model is not well constrained experimentally. The Third aspect is the transformation of ringwoodite to garnet and ferropericlase that occurs in the deep transition zone and which has a significant influence on the velocity structure for EA at the highest temperatures. The magnitude of the 410 km discontinuity is essentially independent of temperature in both MM and EA except for the very highest temperature. For both MM and EA the width decreases with temperature as expected (Helffrich and Bina, 1994; Stixrude, 1997). The magnitude of the post-660 km discontinuity in EA increases with increasing temperature, since the gradient of the shear wave velocity increases significantly as temperature rises. While in MM, the post-660 discontinuity slightly increases in magnitude and deepens with increasing temperature. The 520 km discontinuity becomes weaker with increasing temperature, which may explain why it is difficult to observe globally (Shearer, 1996; Lawrence and Shearer 2006).

1.4 Discussion and Conclusions

The notion of a mechanical mixture suggests a natural metric for exploring compositional heterogeneity in the mantle. Many previous studies have focused on lateral or radial variations in the relative proportions of iron to magnesium, or of silicon to

magnesium (Anderson, 1989; Jeanloz and Knittle, 1989; Stixrude et al., 1992; Trampert, et al., 2004). However, such chemical variations are explored in a largely ad-hoc fashion while the processes that might produce them are uncertain. The advantage of basalt fraction as a compositional metric is that the genetic process is well known: subduction of differentiated oceanic lithosphere. Moreover, dynamical mechanisms have been proposed for segregating basalt from harzburgite in a convecting mantle, including slab delamination, and segregation due to the density contrast between the basalt and harzburgite (Brandenburg and Van Keken, 2007; Christensen and Hofmann, 1994; Davies, 2006; Nakagawa and Buffett, 2005; Ringwood and Irifune, 1988; Xie and Tackley, 2004). Segregation of basalt from harzburgite provides a mechanism for producing radial and lateral variations in basalt fraction.

Within our present understanding of subduction and the differentiated structure of the oceanic lithosphere, it is inevitable that some amount of un-reequilibrated basalt and harzburgite is present in the mantle. In our mechanical mixture model, we have explored the end-member case, corresponding to a mantle that has undergone differentiation at least once, and in which re-equilibration is slow compared to the age of the Earth. Does the mantle lie nearer to this mechanically mixed disequilibrium end-member, or to the equilibrium pyrolitic end-member? Arguments based on experimentally measured chemical diffusivities, suggest that re-equilibration will not be significant over the age of the Earth for the amount of stretching and folding that can be expected in a convecting mantle (Allégre and Turcotte, 1986). However, important uncertainties remain: how much of the mantle has been differentiated? What is the basalt fraction? What might the role of partial melt and water be in enhancing rates of re-equilibration?

Our results provide a means of testing in situ the extent of major element disequilibrium in the mantle based on the significant differences in seismic velocity structure between equilibrium assemblage and mechanical mixture. We argue that the mechanical mixture provides a better match to radial seismological models in the transition zone because it is faster and has a steeper radial velocity gradient.

Comparison to radial seismological models provides tentative evidence of a radial gradient in basalt fraction. Whereas the mechanical mixture matches 1D seismological models of the transition zone significantly better than the equilibrium assemblage, the mechanical mixture is almost certainly too fast in the upper mantle, and too slow in the lower mantle, even accounting for uncertainties in seismological models and the effects of lateral heterogeneity. Our results show that basalt depletion in the upper mantle, and basalt enrichment in the lower mantle, would yield better agreement with seismological models by producing a slower upper mantle and a faster lower mantle. Indeed, just such an enrichment in basalt with increasing depth is seen in several models of mantle convection (Davies, 2006; Nakagawa and Buffett, 2005; Xie and Tackley, 2004).

Our results suggest a powerful thermometer of the transition zone. A remarkable feature of the mechanical mixture model is that the velocity in the transition zone is nearly independent of bulk composition. If this model is representative of the mantle, seismic velocities will be primarily sensitive to temperature. Comparison of the absolute velocity of the mechanical mixture model to that constrained seismically in the transition zone should provide an independent means of determining mantle temperature at depth.

Our results may permit tests of the nature and length scale of lateral variations in composition. In a mechanically mixed mantle we would expect discontinuity structure to

vary laterally, so that it would be best explored at a regional level, in areas where the tectonic history of the mantle is well known. A mechanically mixed mantle should also produce scattering due to the significant velocity contrast between basalt and harzburgite (Stixrude and Jeanloz, 2007).

Bulk composition in mol %

Component	Pyrolite[a]	Basalt[a]	Harzburgite[b]	modified harzburgite[*]
SiO_2	37.76	46.02	35.89	36.00
MgO	48.64	13.31	56.22	56.19
FeO	6.02	6.28	6.04	5.96
CaO	3.08	16.23	0.81	0.27
$AlO_{3/2}$	4.33	18.15	1.05	1.38

[a] Workman and Hart, 2005
[b] Baker and Beckett, 1999
[*] modified Harzburgite under mass and phase balance

Table 1.1, Bulk composition.

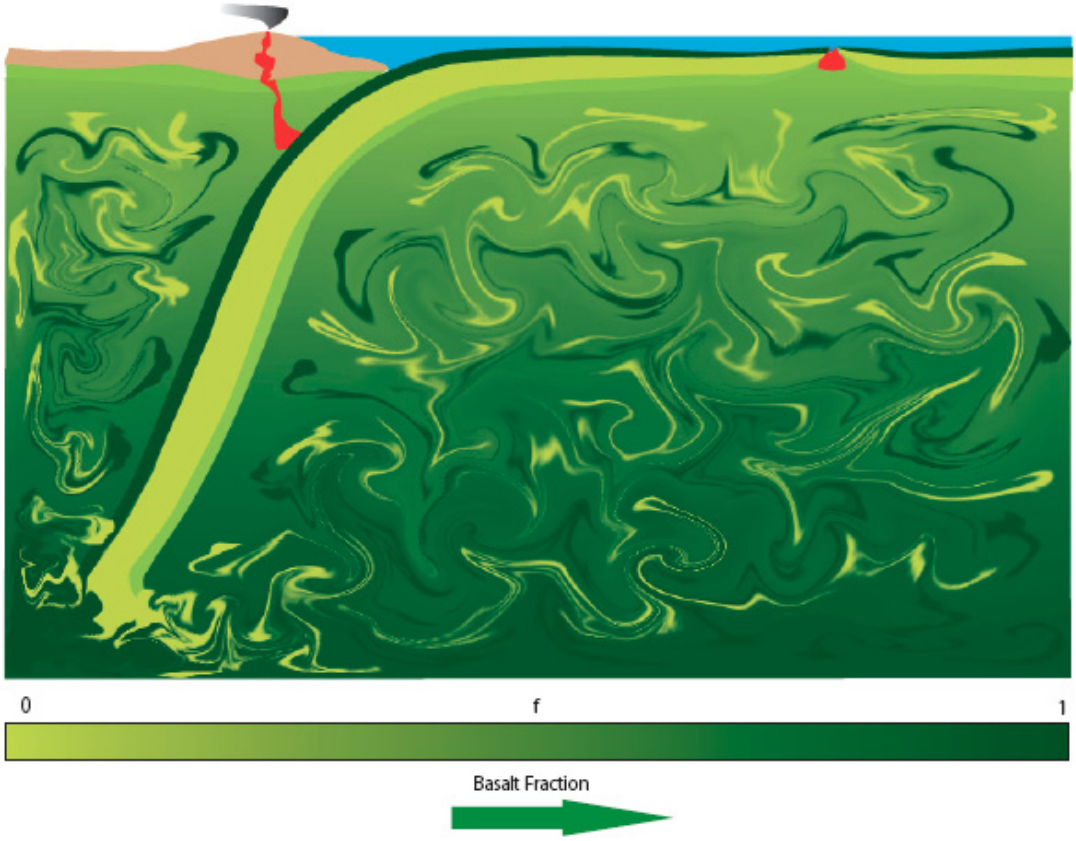

Figure 1.1. Dynamic and chemical processes near (right) mid-ocean ridge and (left) subduction zone. At mid-ocean ridges, because of decompression partial melting, upwelling peridotite (medium green) forms two different chemical layers, basalt (dark green) and the complementary residual harzburgite (light green). At subduction zones, oceanic crust subducts into the mantle where at ~80 km basalt transforms to eclogite, which is 10% denser than harzburgite (olive green). This density difference drives the separation of basalt from the rest part of slab. The end result may be a mantle that is mechanically mixed, with basalt preferentially accumulating in the lower mantle and harzburgite in the upper mantle.

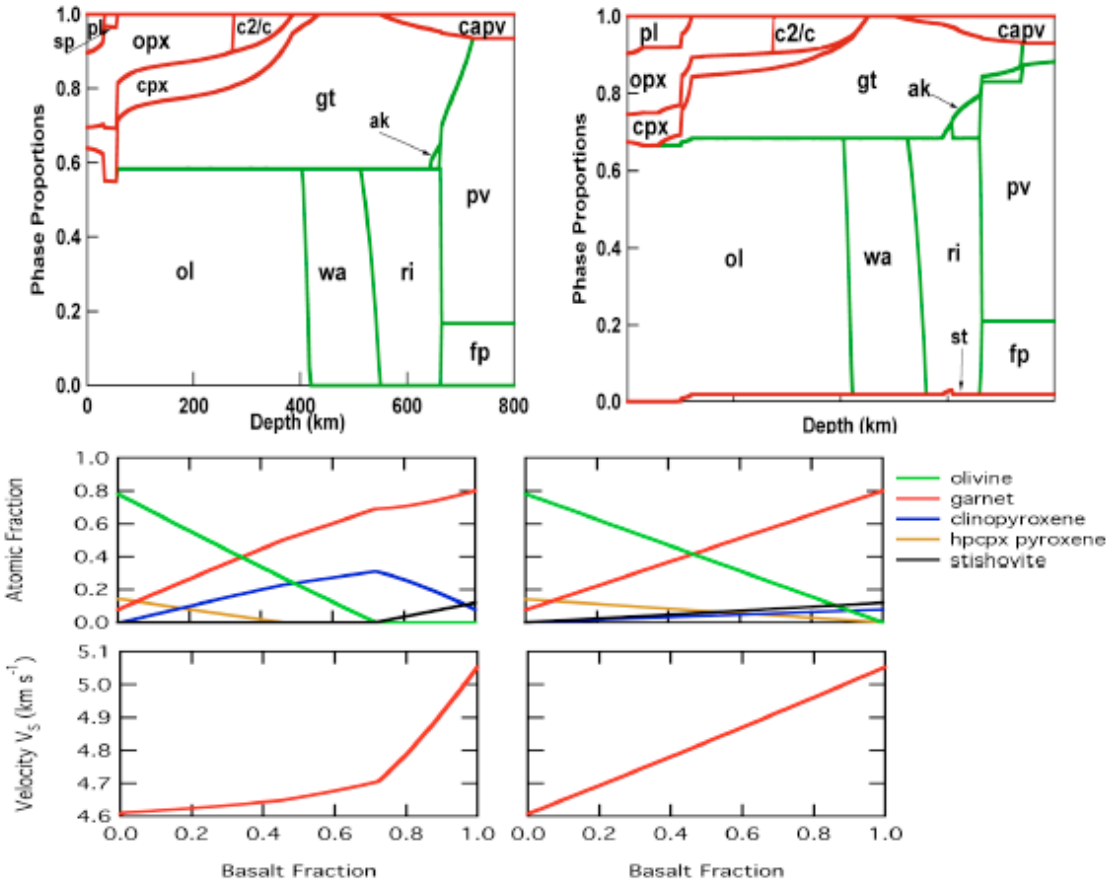

Figure 1.2. Phase proportions (top) and variations of V_S and phase proportions at 10 GPa (300 km depth) and 1600 K (bottom) in EA (left) and MM (right) for the bulk composition shown in Table 1. Phases are: plagioclase (plg), spinel (sp), garnet (gt), olivine (ol), wadsleyite (wa), ringwoodite (ri), orthopyroxene (opx), clinopyroxene (cpx), high pressure Mg-rich clinopyroxene (C2/c), akimotoite (ak), stishovite (st), Ca-silicate perovskite (capv), Mg-rich silicate perovskite (pv), and ferropericlase (fp). Phase proportions in the bottom panel are for olivine (green), garnet (red), cpx (blue), C2/c (gold), and st (black).

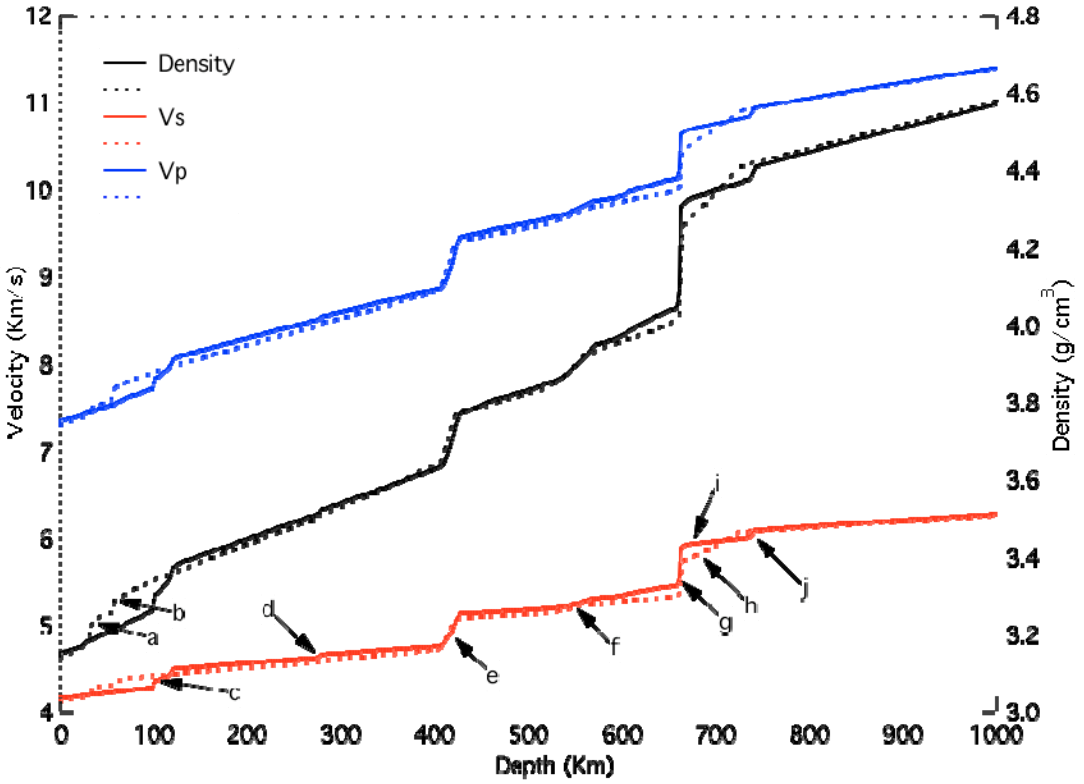

Figure 1.3. Seismic wave velocity and density as function of pressure for the mechanical mixture (solid line, denoted as MM) and equilibrium assemblage (dashed line, denoted as EA) along an adiabat with potential temperature 1600 K for identical bulk compositions (basalt fraction 17.6%). The mechanical mixture is faster (around 0.06 km/s in V_S and 0.08 km/s in V_P) and denser than the equilibrium assemblage. The gradient of velocity in the transition zone is steeper for the mechanical mixture. The other prominent difference is that the 660 km discontinuity is immediately followed by a high gradient zone in EA, due to the gradual dissolution of garnet into perovskite, which does not appear in MM. The letters label the following phase transformations, which occur in both EA and MM unless otherwise noted: a) plg=sp (EA); b) sp=gt (EA); c) plg=gt (MM); d) opx=C2/c; e) ol=wa; f) wa=ri; g) ri=pv+fp; h) gt=pv (EA); j) gt=pv (MM).

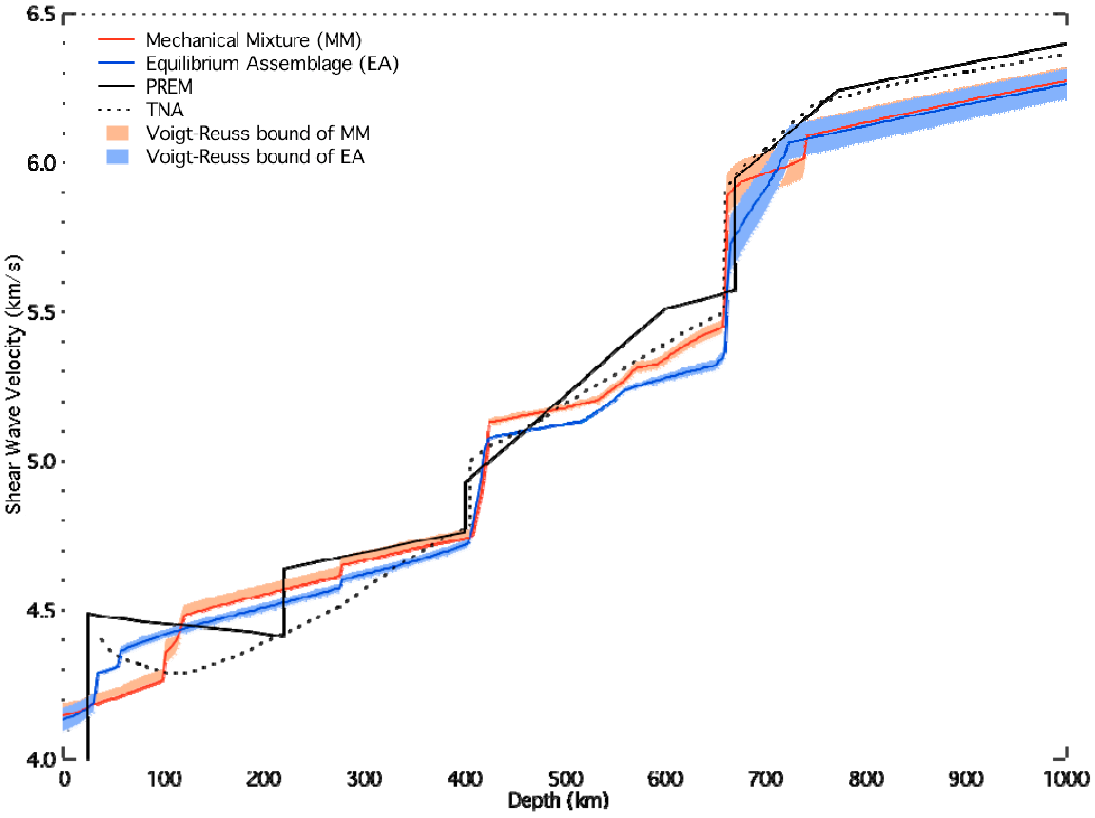

Figure 1.4. Shear wave velocity profiles for the two compositional models for identical geotherms and bulk compositions (1600 K and 17.6% basalt fraction). The shading corresponds to the Voigt-Reuss bounds. The bold lines represent the Voigt-Reuss-Hill averages for MM (red) and EA (blue). Black solid line is the PREM profile (Dziewonski and Anderson, 1981) and dashed line TNA (Grand and Helmberger, 1984).

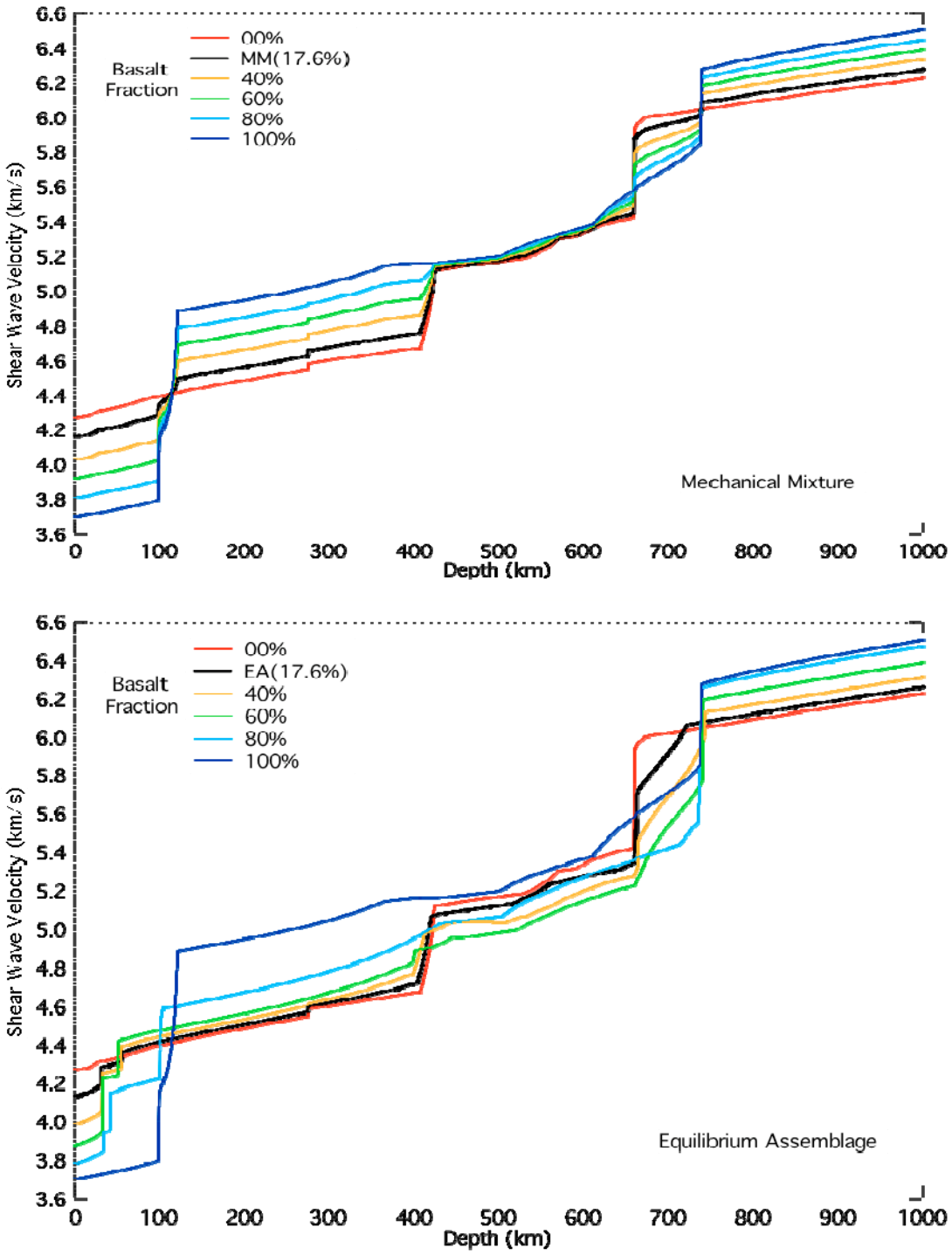

Figure 1.5. Profile of shear wave velocity V_S as a function of depth with different basalt fractions (0-100%) for the two models: (Top) mechanical mixture and (bottom) equilibrium assemblage. All calculations are along the 1600 K adiabat of EA pyrolite.

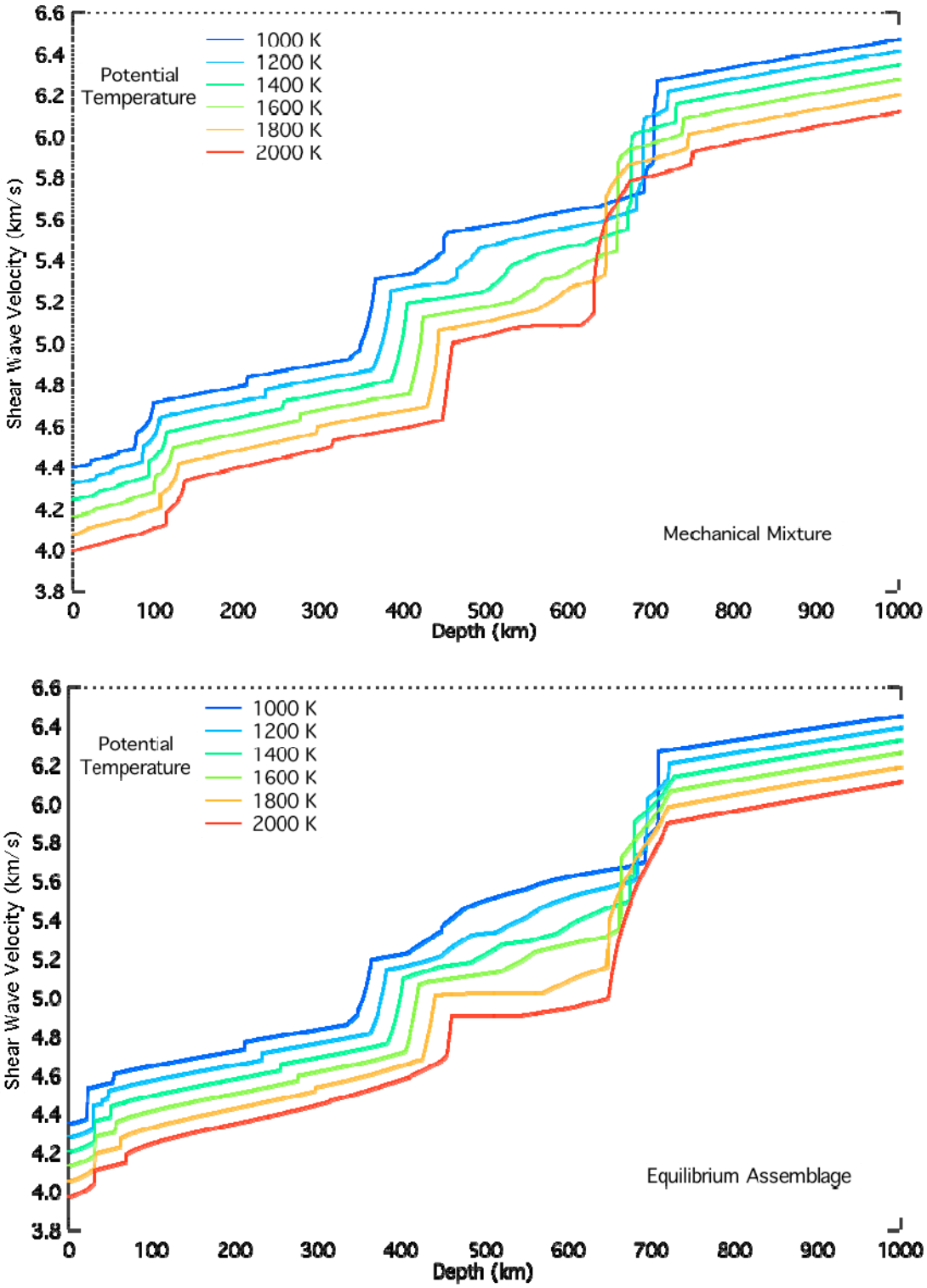

Figure 1.6. Shear wave seismic velocity profiles along adiabats of different potential temperatures (1000 K-blue to 2000 K (red) for (top) MM and (bottom) EA. The bulk composition of the two models is identical (f=17.6 %).

1.5 REFERENCES

Allégre, C.J., Turcotte, D.L., 1986. Implications of a two-component marble-cake mantle. Nature 323, 123-127.

Anderson, D.L., Bass, J.D., 1986. Transition Region Of The Earth Upper Mantle. Nature, 320, 321-328.

Anderson, D.L., 1987. Thermally Induced Phase-Changes, Lateral Heterogeneity of the Mantle, Continental Roots, and Deep Slab Anomalies. J. Geophys. Res.-Solid Earth and Planets. 92,13968-13980.

Anderson, D.L., 1989. Theory of the Earth. Blackwell Scientific Publications, Boston, 147-177.

Baker, M.B., Beckett, J.R., 1999. The origin of abyssal peridotites: a reinterpretation of constraints based on primary bulk compositions. Earth Planet. Sci. Lett. 171, 49-61.

Bass, J. D., 1995. Elasticity of minerals, glasses, and melts, in Mineral Physics and Crystallography, in: Ahrens, T.J., A handbook of physical constants, AGU, Washington, D.C. pp. 465-63.

Brandenburg, J.P., Van Keken, P.E., 2007. Deep storage of oceanic crust in a vigorously convecting mantle. J. Geophys. Res. 112, B06403. doi: 10.1029/2006JB004813.

Callen, H.B., 1960. Thermodynamics. John Wiler & Sons, New York.

Chen, C.Y., Frey, F.A., Garcia, M.O., et al. 1991. The tholeiite to alkalic basalt transition at Haleakala Volcano, Maui, Hawaii. Contributions to Mineralogy and Petrology 106, 183-200.

Christensen, U., Hofmann, A.W., 1994. Segregation of subducted oceanic crust in the mantle. J. Geophys. Res. 99, 19867-19884.

Davies, G.F., 2006. Gravitational depletion of the early Earth's upper mantle and the viability of early plate tectonics. Earth Planet. Sci. Lett. 243, 376-382.

Deuss, A., Redfern, S.A.T., Chambers, K.,Woodhouse, J.H., 2006. The Nature of the 660-Kilometer Discontinuity in Earth's Mantle from Global Seismic Observations of PP Precursors. Science 311, 198-210.

Dziewonski, A. M., Anderson, D. L., 1981. Preliminary reference Earth model. Phys.Earth Plant. Inter. 25, 297-356.

Farber, D.L., Willams, Q., Ryerson, F.J., 1994. Diffusion in Mg_2SiO_4 polymorphs and chemical heterogeneity in the mantle transition zone. Nature 371, 693-695.

Francis, D., 1987. Mantle-melt interaction recorded in spinel lherzolite xenoliths from the Alligator lake Volcanic complex, Yukon, Canada. J. Petrology 28, 569-597.

Frey, F.A., Green, D.H., Roy, S.D., 1978. Integrated models of basalt petrogenesis: A study of Quartz Tholeiites to Olivine melilitites from south eastern Australia utilizing geochemical and experimental petrological data. J. Petrology 19, 463-513.

Helffrich G., Bina C.R., 1994. Frequency-Dependence Of The Visibility And Depths Of Mantle Seismic Discontinuities. Geophys. Res. Lett. 21, 2613-2616.

Hirose, K., Takafuji, N., Sata, N., Ohishi, Y., 2005. Phase transition and density of subducted MORB crust in the lower mantle. Earth Planet. Sci. Lett. 237, 239-251.

Hirschmann, M.M., Stolper, E.M., 1996. A possible role for garnet pyroxenite in the origin of the "garnet signature" in MORB. Contributions To Mineralogy And Petrology 124 (2), 185-208.

Irifune,T., 1993. Phase transformation in the earth's mantle and subducting salbs: Implications for their compositions, seismic velocity and density structures and dynamics. Island Arc 2, 55-71.

Ita, J. J., and Stixrude, L., 1992. Petrology, elasticity and composition of the transition zone. J. Geophys. Res. 97, 6849-6866.

Jeanloz, R., Knittle E., 1989. Density and composition of the lower mantle. Philosophical Transactions of the Royal Society of London 328, 377-389.

Kellogg, J. B., Jacobsen, S.B., O'Connell, R.J., 2002. Modeling the distribution of isotopic ratios in geochemical reservoirs. Earth Planet. Sci. lett. 204, 183-202.

Lawrence, J. F., Shearer, P. M., 2006. Constraining seismic velocity and density for the mantle transition zone with reflected and transmitted waveforms. Geochem. Geophys. Geosyst. 7, Q10012, doi:10.1029/2006GC001339.

Mattern, E., Matas, J., Ricard, Y., Bass, J., 2005. Lower mantle composition and temperature from mineral physics and thermodynamic modelling. Geophys. J. Int. 160 (3): 973-990.

Mckenzie, D., Bickle, M.J., 1988. The volume and composition of melt generated by extension of the lithosphere. J. Petrology 29, 625-679.

Morgan, J.P., Morgan, W.J., 1999. Two-stage melting and the geochemical evolution of the mantle: a recipe for mantle plum-pudding. Earth Planet. Sci. Lett. 170 (3): 215-239.

Nakagawa, T., Buffett, B.A., 2005. Mass transport mechanisms between the upper and lower mantle in numerical simulations of thermo-chemical mantle convection with multi-component phase changes. Earth Planet. Sci. Lett. 230, 11-27.

Revenaugh, J., Jordan, T.H., 1991. Mantle layering from ScS reverberations 3. the upper mantle. J. Geophys. Res.-Solid Earth 96, 19,781-19,810.

Ringwood, A. E., 1966. The chemical composition and origin of the earth, In: Hurley,P.M., Advances **in** Earth Science , Cambridge, Mass.: M.I.T. Press, 287-356.

Ringwood, A. E., 1969. Composition and evolution of the upper mantle, in: Hart, P.J., The Earth's Crust and upper mantle: structure, dynamic process, and their relations to deep-seated geological phenomena. Geophys. Mongr. Ser. 13, Washington, D. C., 1-17.

Ringwood, A. E., 1979. Origin of the earth and moon. Springer-Verlag New York, Inc, New York.

Ringwood, A.E., Irifune, T., 1988. Nature of the 650–km seismic discontinuity: implications for mantle dynamics and differentiation. Nature 331, 131-136.

Shearer, P. M., 1996. Transition zone velocity gradients and the 520-km discontinuity. J. Geophys. Res. 101, 3053–3066.

Simmons, N.A., Gurrola, H., 2000. Multiple seismic discontinuities near the base of the transition zone in the Earth's mantle. Nature 405, 559-562.

Sobolev, A.V., Hofmann A.W., Kuzmin D.V., et al., 2007. The amount of recycled crust in sources of mantle-derived melts. Science 316, 412-417.

Stixrude, L., Hemley, R.J., Fei, Y., Mao, H.K., 1992. Thermoelasticity of Silicate Perovskite and Magnesiowüstite and Stratification of the Earth's Mantle. Science 257, 1099-1101.

Stixrude, L., 1997. Structure and sharpness of phase transitions and mantle discontinuities. J. Geophys. Res.-Solid Earth.102, 14835-14852.

Stixrude, L., Lithgow-Bertelloni, C., 2005a. Mineralogy and elasticity of oceanic upper mantle: Origin of the low velocity zone. J Geophys. Res. 110, B03204, doi:10.1029/2004JB002965

Stixrude, L., Lithgow-Bertelloni, C., 2005b. Thermodynamics of mantle minerals I: Physical properties. Geophys. J. Int. 162, 610-632.

Stixrude, L., Lithgow-Bertelloni, C., 2007. Influence of phase transformations on lateral heterogeneity and dynamics in Earth's mantle. Earth Planet. Sci. Lett., doi:10.1016/j.epsl.2007.08.027.

Stixrude, L., Jeanloz, R., 2007. Constraints from mineral physics on seismological models, Treatise on Geophysics, G. Schubert (ed.), Elsevier, Amsterdam, in press.

Trampert, J., Deschamps, F., Resovsky, J., Yuen, D., 2004. Probabilistic tomography maps chemical heterogeneities throughout the lower mantle. Science 306, 853-856.

Watt, J. P., Davies, G. F., O'Connell, R. J., 1976. The elastic properties of composite materials. Rev. Geophys. Space Phys. 14, 541-563.

Weidner, D.J, 1985. A mineral physics test of a pyrolite mantle. Geophys. Res. Lett. 12, 417-420.

Williams, Q., Revenaugh J., 2005. Ancient subduction, mantle eclogite, and the 300 km seismic discontinuity. Geology 33 (1): 1-4.

Woodland, A. B., 1998. The orthorhombic to high-p monoclinic phase transition in Mg-Fe pyroxenes: Can it produce a seismic discontinuity?, Geophys. Res. Lett. 25, 1241-1244.

Workman, R.K., Hart, S. R., 2005. Major and trace element composition of the depleted MORB mantle (DMM). Earth Planet. Sci. Lett. 231, 53-72.

Xie, S., Tackley, P., 2004. Evolution of U-Pb and Sm-Nd systems in numerical models of mantle convection and plate tectonics. J. Geophys. Res. 109, 10.1029/2004JB003176.

Xu, X., Lithgow-Bertelloni, C., Conrad, C.P., 2006. Global reconstructions of Cenozoic seafloor ages: Implications for bathymetry and sea level. Earth Planet. Sci. Lett. 243, 552-564.

Yamazaki, D., Kato, T., Yurimoto, H., et al., 2000. Silicon self-diffusion in $MgSiO_3$ perovskite at 25 GPa, Phys. Earth Plant. Inter. 119: 299-309.

Chapter II
Is the asthenosphere a plumeyard? Super-adiabatic gradients in the low velocity zone of Western North America

2.1 Introduction

The Earth's upper mantle beneath the lithosphere is a distinctive seismic structure, with low and laterally heteregenous seismic velocities *(e.g. Grand and Helmberger, 1984)* and high attenuation, which was first identified as the low-velocity zone by *Gutenberg (1959)*. This structure is a persistent feature of global and local seismic models. It seems to coincide with a proposed low-viscosity asthenosphere, which is likely essential as an enabler of plate motions *(Richard et al., 2001; Tackley,2000)*.

The low velocity zone is characterized by negative velocity gradients, expected when the thermal gradient is large enough that the effects of temperature on velocity are greater than those due to compression *(Stixrude and Lithgow-Bertelloni, 2005a)*. To best understand the origin of the low velocity zone it is important to quantitatively analyze the absolute velocities and the gradient of velocity.

Stixrude and *Lithgow-Bertelloni (2005a)* used a self-consistent computation of phase equilibria and physical properties for a pyrolitic composition. They concluded that a low-velocity zone is the natural consequence of the change from a thermal boundary layer to an adiabatic interior and the effects of pressure and temperature on the elastic wave velocity of subsolidus mantle assemblage. However, they did not

present a quantitative estimation of the geotherm that would best match existing seismic models.

Stixrude and Lithgow-Bertelloni (2005a) also showed that it was not possible to explain the low-velocity zone without accounting for attenuation. Shear dissipation is greatest at depths between 80-200 km in the upper mantle, where the quality factor Q is less than 100 (Durek and Ekstrom, 1994; Dziewonski and Anderson, 1981; Romanowicz, 1995; Romanowicz and Durek, 2000; Widmer et al., 1991). The interpretation for the high attenuation is viscoelastic behavior, which is the transition from elastic behavior through essentially anelastic into predominantly viscous deformation, of ultramafic materials at high temperature (Jackson et al., 2002). Jackson et al. (2002) quantified the sensitivity of Q to variations in grain size, temperature, and frequency.

Partial melting has also been invoked to explain the origin of the low-velocity zone (Anderson and Sammis, 1969; Green and Liebermann, 1976; Lambert and Wyllie, 1968; Ringwood, 1969; Sato et al., 1989). Partial melt can only exist if the mantle temperature exceeds the solidus. If partial melt exists in the low velocity zone beyond the immediate vicinity of the ridge, it may be thermodynamically stabilized by small amounts of water. Until recently, this hypothesis was difficult to test because the lowering of the mantle solidus due to small amounts (few 100 ppm by mass) of water was poorly constrained.

Changes in major element chemical composition could also contribute to the formation of low-velocity zone. However, within a plausible range of variations in bulk composition this seems unlikely to decrease velocity enough to match the velocity in the low-velocity zone (*Stixrude and Lithgow-Bertelloni*, 2005a).

The limitation of previous studies is that they have not considered all factors simultaneously. The calculations presented here account for changes in temperature, grain size, bulk composition, and others to explore potential causes of the low-velocity zone. It takes advantage of the vast development in the knowledge of velocities of upper mantle minerals by integrating the latest experimental data.

I focus mainly on the upper mantle beneath Western North America. I find the geothermal profile of the upper mantle that best fits two 1-D shear waves profiles: WNA (*Merrer et al., 2007*) and TNA *(Grand and Helmberger, 1984)* (Figure 2.1), both of which are constrained with fundamental mode and overtone surface waves and show a prominent low velocity zone at depth of 50-250 km beneath Western North America (Figure 2.1.c), using a self-consistent thermodynamic model for two pyrolitic bulk compositions (Stixrude and Lithgow-Bertelloni, 2005a, 2005b), explained in detail in Chapter 1. Considering the extraction of basalt from MORB source, I also explored the effect of variation of bulk composition with the two end-member models discussed in Chapter 1. The following sections outline the method for the self-consistent computation of phase equilibria and physical properties by incorporating the effect of attenuation.

2.2 Methodology

Shear wave velocity is influenced by bulk composition, temperature, pressure, attenuation, water, and partial melting. The relative importance of these effects are difficult to estimate a priori. We take a different approach, recognizing that to the extent that these various effects are important, they will be reflected in seismological observations, and in seismic models.

2.2.1 Thermodynamic method

I apply a newly developed thermodynamic model (*Stixrude and Lithgow-Bertelloni*, 2005a, 2005b), which enables self-consistent computation of physical properties and phase equilibria and extensively described in previous work (*Stixrude and Lithgow-Bertelloni*, 2005b, *Xu et al*., 2008). Based on fundamental thermodynamic relations (*Callen*, 1960), this model used Legendre transformations to capture complete information of all equilibrium states, including all phase equilibria and physical properties, at given temperature, pressure, and bulk composition. The calculation consists of three steps: 1) determine the proportions and compositions of coexisting phases at given pressure, temperature, and bulk composition by minimizing the Gibbs free energy with respect to the amounts of species to define the equilibrium state of assemblage; 2) taking stress and temperature derivatives of Gibbs free energy to describe physical properties of each individual phase; 3) calculate the physical properties of assemblage via Voigt-Reuss-Hill average (Watt et al., 1976).

In these calculations, as in Chapter 1, a simplified model of mantle with six components: CaO, FeO, MgO, SiO_2, Al_2O_3, Na_2O, and 45 mantle species is proposed. Depleted Mid-Ocean Ridge-Basalt Mantle (DMM) (Workman and Hart, 2005) is used as our estimation of bulk composition of the mantle. I approximate the composition of basalt as the MORB model of Workman and Hart (2005). The composition of Harzburgite is modified based on the most recent depleted composition model (Baker and Beckett, 1999). Xu et al. (2008) showed that Equilibrium Assemblage (EA) and Mechanical Mixture (MM) yield substantially different seismic velocities for the identical bulk

composition. So the effect of variations in the bulk composition, as measured by the basalt fraction, is also explored based on EA and MM.

2.2.2 Attenuation

The shear attenuation Q of the upper mantle has been extensively studied (Figure 2.2) with data from body waves, normal modes, and surface waves (Anderson and Archambeau, 1966; Buland and Gilbert, 1978; Deschamps, 1977; Gilbert and Dziewonski, 1975; Jobert and Roult, 1976; Kanamori, 1970; Romanowicz, 1995; Romanowicz and Durek, 2000; Roult, 1975; Sailor and Dziewonski, 1978; Stein and Geller, 1978) and multiple ScS (Chan and Der, 1988; Flanagan and Wiens, 1990; Kovach and Anderson, 1964; Lay and Wallace, 1983; Nakanishi, 1979; Sipkin and Jordan, 1980; Yoshida and Tsujiura, 1975). Besides observational constraints, theoretical and experimental studies are also developed to explore attenuation in the mantle (Faul and Jackson, 2005; Gribb and Cooper, 1998; Jackson et al., 1992; Jackson et al., 2002; Tan et al., 1997; Tan et al., 2001). Here I proposed two methods to approximate attenuation.

Q based on seismological models. In this approach, I use the seismic model QR19 (Romanowicz, 1995) as reference of our attenuation model, which is a global three-dimensional model of shear attenuation in the mantle. I assume that shear attenuation depends on temperature as

$$Q(P,T) = Q_0(P)\exp(\alpha\frac{E^*}{R}(\frac{1}{T}-\frac{1}{T_0}) \tag{2.1}$$

where $Q_0(P)$ is the spherically averaged part of QR19 (Romanowicz, 1995), P is pressure, T is temperature, T_o is reference temperature, taken to be the 1600K isentrope, R is gas constant, the frequency exponent α =0.26, and the activation energy E^* =424 kJ mol^{-1} (Jackson et al., 2002).

Q based on experiment. Experimental data has been quantitatively described by a Burgers model solid (Faul and Jackson, 2005). The energy dissipation Q^{-1} is calculated as follows:

$$Q^{-1} = \frac{J_2(\omega)}{J_1(\omega)} \tag{2.2}$$

with

$$J_1(\omega, d, T, P) = J_U(P)\{1 + \delta \ln J_U + \frac{\alpha_Q \Delta}{\tau_H^{\alpha_Q} - \tau_L^{\alpha_Q}} \int_{\tau_L}^{\tau_H} \frac{\tau^{\alpha_Q - 1}}{1 + \omega^2 \tau^2} d\tau\} \tag{2.3}$$

and

$$J_2(\omega, d, T, P) = J_U(P)\{\frac{\omega \alpha_Q \Delta}{\tau_H^{\alpha_Q} - \tau_L^{\alpha_Q}} \int_{\tau_L}^{\tau_H} \frac{\tau^{\alpha_Q}}{1 + \omega^2 \tau^2} d\tau + \frac{1}{\omega \tau_M}\} \tag{2.4}$$

where $J_U(P)$ is the unrelaxed compliance, given by the reciprocal of the unrelaxed (elastic) shear modulus G_U, ω, d, T, P are angular frequency, grain size, absolute temperature and pressure, respectively, α_Q is the frequency exponent, Δ is a parameter that measures the anelastic relaxation strength, and $\delta \ln J_U$ is the fractional adjustment to J_U in the viscoelastic regime

$$\delta \ln J_U = (\frac{\partial \ln J_U}{\partial T})_R (\frac{d}{d_R})^{-m_J} (T - T_R) \tag{2.5}$$

where subscript R refers to reference. The lower and upper cutoff time (τ_L, τ_H) and Maxwell relaxation time (τ_M) are calculated as

$$\tau_i = \tau_{iR}\left(\frac{d}{d_R}\right)^m \exp\left\{\frac{E^* + PV^*}{R}\left(\frac{1}{T} - \frac{1}{T_R}\right)\right\} \tag{2.6}$$

All the parameters are listed in Table 1. The period (s) in the calculations is approximately scaled to 3/4.2 depth (km) as appropriate for surface waves (Forsyth, 1999).

The effect of pressure is modeled as a constant activation volume by which the relaxation times increase with increasing pressure. As there are no experimental constraints on V^* for attenuation, we adopt a range of values representative of diffusion and dislocation creep (6-12 cm^3/mol). The grain size of the mantle is also poorly constrained, and so we adopt a range of values consistent with constraints from xenoliths and the comparison of post-glacial rebound with experimental measurements of viscosity (1-10 mm) (Jackson et al., 2002).

2.2.3 Anisotropic correction

The two seismic models under investigation are polarized: WNA is based on fundamental and higher mode Rayleigh waves and is therefore sensitive to the vertically polarized shear wave velocity. TNA is based on first arriving S and SS phases and is therefore primarily sensitive to the (faster) horizontally polarized shear wave velocity. In order to compare with our thermodynamic calculations, which produce the isotropically averaged Voigt-Reuss-Hill shear wave velocity, we must first correct the seismic models

for anisotropy. We estimate the relationship between the Voigt-Reuss-Hill velocity (V_S) and the horizontally (V_{SH}) and veritcally (V_{SV}) polarized velocities as

$$V_S = \frac{V_{SH} + V_{SV}}{2} \tag{2.7}$$

The relationship between V_{SH} and V_{SV} is described as

$$\xi = \left(\frac{V_{SH}}{V_{SV}} \right)^2 \tag{2.8}$$

where we take the value of ξ versus depth from the 4-20 Ma model of Nishimura and Forsyth's table (Table 1) (1989).

2.3 Results

2.3.1 Burgers Solid Model

Inverting WNA yields a mushroom-shaped geotherm in the range of 100-250 km depth (figure 2.3), which corresponds to the depth of LVZ or asthenosphere. The temperature along the geotherm increases with increasing depth to 200 km, and then decreases with increasing depth at greater depths. The inverted geotherm is hotter than the 1600 K adiabat in the region of 150-220 km: 40-80 K hotter at its peak (200 km), but substantially colder than dry and wet solidi. The predicted Q is smaller than the spherically averaged part of QR19 by 20-30. The high attenuation region is somewhat wider than in QR19 (50-250 km vs. 100-250 km, respectively). We also fit to WNA using EA as the starting compositional model (Figure 3.4). Compared with M, there is no obvious difference. Except that the inverted geotherm with EA has larger deviations form 1600 K adiabat at depths greater than 250 km.

The same set of parameter for the Burgers model is applied to TNA (figure 2.5). The most notable features is that there is a small difference between EA fitting and MM fitting. The increasing trend above 100 km in TNA is much steeper than the geotherm obtained from fitting to WNA. This is explained by the steeper gradient in the TNA seismic model. But between the depth of 100 km and 250 km, the inverted geotherm is much flatter and colder than that obtained from WNA so that it is barely hotter than the 1600 K adiabat, and peaks at 120 km. The geotherm inverted by fitting to TNA shows a larger deviation away from 1600 K adiabat deeper than 250 km. Compared with the predicted Q from the WNA fits, Q is 5-10 less above 150 km, and 5-10 larger than WNA deeper 150 km. The depth range of the high attenuation zone is the same,

Since the activation volume and grain size in the upper mantle is not well constrained, I explore the influence of activation volume (figure 2.6) and grain size (2.7) on the inverted geotherms. In both cases, the pattern of variation of Q with depth are not changed much, although the temperature and absolute value of Q differ. The peak in the inverted geotherm is deepened with higher activation volume (figure 2.6). Higher activation volume also implies a higher Q. In the LVZ, Q is still smaller than QR19 with all three activation volumes.

The influence of grain size is not as strong as that of activation volume (figure 2.7). The variation of Q and the inverted geotherm through the upper mantle for different grain size is constant with depth and small: a 15 K hotter geotherm and values of Q increasing by 10 for doubling of the grain size.

2.3.2 Q based on QR19

Inversions using Q based on QR19 also shows a beautiful mushroom-shaped geotherm (figure 2.8). For MM the inverted geotherm for WNA is 100 K hotter than when using the Burgers model (figure 2.3). Therefore, after attaining its peak at 160 km, the predicted geotherm falls from 1800 ± 40 K back to the 1600 K adiabatic values at 250 km. It overlaps with the 1600 K adiabat when deeper than 250 km. In the LVZ, the predicted geotherm is now close to the wet solidus for 200 ppm H_2O, although there is a sudden change in the inverted geotherm between 50 and 100 km depth. The predicted Q fits QR19 quite well, except right at the LVZ, where it is ~18 smaller than QR19. The results with EA are very similar (figure 2.9), although there are also some important differences. The geotherm is now much closer to the wet, and between 50-100 km, there is overlap between the predicted geotherm and the wet solidus. At depths greater than 250 km, deviation from 1600 K adiabat persists so that it is not parallel and there is no overlap.

Inversion from TNA (figure 2.10) shows a distinct geothermal structure compared with the WNA fits with MM using the Burgers model (figure 2.3). MM and EA model yield similar geotherms. Both of them increase sharply between 50 km and 80 km. Below that the geotherm is flat until 300 km depth, although 50-100 K hotter than the 1600 K adiabat.

2.4 Discussion and conclusions

2.4.1 General

With two approximations of attenuation, our modeling, based on new experimental data and self-consistent calculation of physical properties and phase

equilibria, seeks to produce reasonable fits to the regional seismic models for Western North America: TNA and WNA. For a range of different compositional models and different parameters, i.e., activation volume and grain size, all inversion results show similar features: a low Q zone, with values of Q lower than those of the spherically averaged model QR19, as anticipated for the tectonically young study area; a mushroom-shaped geotherm in the low velocity zone and a geotherm approximately parallel to the adiabatic geotherm with potential temperature 1600 K for depths greater than 250 km. However, important differences arise for the variations in model parameters, whose geophysical implications I explore below.

2.4.2 Attenuation Model

As descripted in the methodology section, QR19 (Romanowicz, 1995) is a globally averaged model for the shear attenuation in the mantle, whereas TNA and WNA are models of a tectonically young active area. In the inversions with Q based on QR19, we assume a reference temperature equal to the adiabat. This is probably not the most appropriate as the globally averaged geotherm will have a thermal boundary layer. This mis-match between the assumed reference temperature and the global average that QR19 represents is the most likely explanation of the regions of the inverted geotherms that cross the solidus.

2.4.3 Grain size and activation volume

Comparing the results of Burgers model and Q(T), the grain size and activation volume in the upper mantle is predictable. Previous studies suggest that the representative

grain size is 1-10 mm in the upper mantle (Jackson et al., 2002). But it is clear from Figure 2.7 that the geotherm is not sensitive to grain size. Although grain size increases is expected with depth (Faul and Jackson, 2005, Hirth and Kohlstedt, 2003), we see that the change in the temperature will be less than 50 K for the expected variation in grain size. This implies that the estimated grain size of 1-10 mm, is a good approximation, especially for an adiabat 50-100 K colder.

2.4.4 Plumeyard

As described above, all the inverted geotherms yield a characteristic mushroom-shaped in the low velocity zone, which is coincident with the depth of asthenosphere. In the low velocity zone, temperature starts to deviate away from the 1600 K adiabat to hotter temperatures at depths greater than 150 km. The highest temperatures obtained reach ~1850 K between 150-200 km depth. At depths greater than 250 km, where the asthenosphere ends, the geotherm falls back (80-100 K colder than 1600 K adiabatic) and is parallel to the adiabatic until the 410 km discontinuity.

Morgan et al. (1995) gave a potential interpretation to this geothermal structure: the asthenospheric layer is entirely fed from below by upwelling plumes and loses equal mass by accretion to the overlying oceanic lithosphere (figure 2.11). This will lead to ~150-300 K (Davies, 1988) excess in temperature in the depth range of 100-300 km (Widmer et al., 1991; Morgan et al., 1995).

The mushroom shaped LVZ geotherm explains another difficulty found in the study of Stixrude and Lithgow-Bertelloni (2005a). They found that the velocity gradient seen in seismic models below the low velocity zone (~200-400 km) was much too high to

explain with a chemically homogeneous, adiabatic mantle. In the plumeyard picture, the temperature decreases with increasing depth below the asthenosphere, providing a natural explanation of these high velocity gradients.

2.4.5 Water effect and partial melting

All the results presented, with either TNA or WNA show that the geotherms fall below the dry solidus and the 200 ppm H_2O wet solidus. However partial melting with water can't be ruled out in the upper mantle. The inverted geotherms for both TNA and WNA with Q based on QR19 come very close to the 200 ppm H_2O wet solidus in the range of 50-100 km, which is a potential depth for partial melting. The 'abnormal' increase of the geotherm in that range suggests that partial melting may occurat that depth. We think a more likely explanation is that the super-solidus portions of the inverted geotherm are an artifact of the mis-match between the reference temperature and the globally averaged model QR19 mentioned above. It is possible that with a different reference temperature in Eq. 2.1, one that included a thermal boundary layer, the super-solidus regions of the inverted geotherm would be absent, as they are for inversions with the experimentally based Q.

Table 2.1 Parameters of the Burgers model

Parameter	Unit	Values	Uncertainty
d_R	m	1e-5	
T_R	K	1223	
J_U	GPa^{-1}	0.0149	0.0001
$\partial \ln J_U / \partial T$	K^{-1}	9.1e-4	7e-5
1.4			
α_Q		0.270	0.008
0.003981			
τ_H		5.26e6	1.55e6
τ_M		4.31e6	2.38e6
m_A		1.09	0.05
m_J		0.16	0.02
m_V		2.1	0.4
E^*	$J\ mol^{-1}$	5.05e5	0.5e5
V^*	$m^3\ mol^{-1}$	1.2e-5	
V^* [a]	$m^3\ mol^{-1}$	1.5-2.5e-5	
d[b]	m	1-10e-3	

Parameters from Faul and Jackson (2005), except
a, Karato and Wu (1993)
b, Jackson et al. (2002)

Table 2.2, Transversely anisotropic model from Nishimura and Forsyth (1988)

Depth(km)	§	uncertainty)	Depth(km	§	uncertainty
15	1.0260	0.0284	215	0.9973	0.0292
25	1.0338	0.0272	225	0.9951	0.0293
35	1.0354	0.0272	235	0.9937	0.0293
45	1.0369	0.0274	245	0.9928	0.0293
55	1.0394	0.0276	255	0.9923	0.0294
65	1.0422	0.0277	265	0.9922	0.0295
75	1.0448	0.0277	275	0.9924	0.0295
85	1.0466	0.0277	285	0.9927	0.0296
95	1.0472	0.0277	295	0.9931	0.0297
105	1.0465	0.0278	305	0.9936	0.0297
115	1.0442	0.0280	315	0.9942	0.0298
125	1.0406	0.0283	325	0.9947	0.0298
135	1.0360	0.0286	335	0.9953	0.0299
145	1.0305	0.0288	345	0.9958	0.0299
155	1.0247	0.0290	355	0.9963	0.0299
165	1.0189	0.0292	365	0.9967	0.0299
175	1.0133	0.0292	375	0.9971	0.0299
185	1.0082	0.0293	385	0.9976	0.0300
195	1.0038	0.0293	395	0.9984	0.0300
205	1.0002	0.0292			

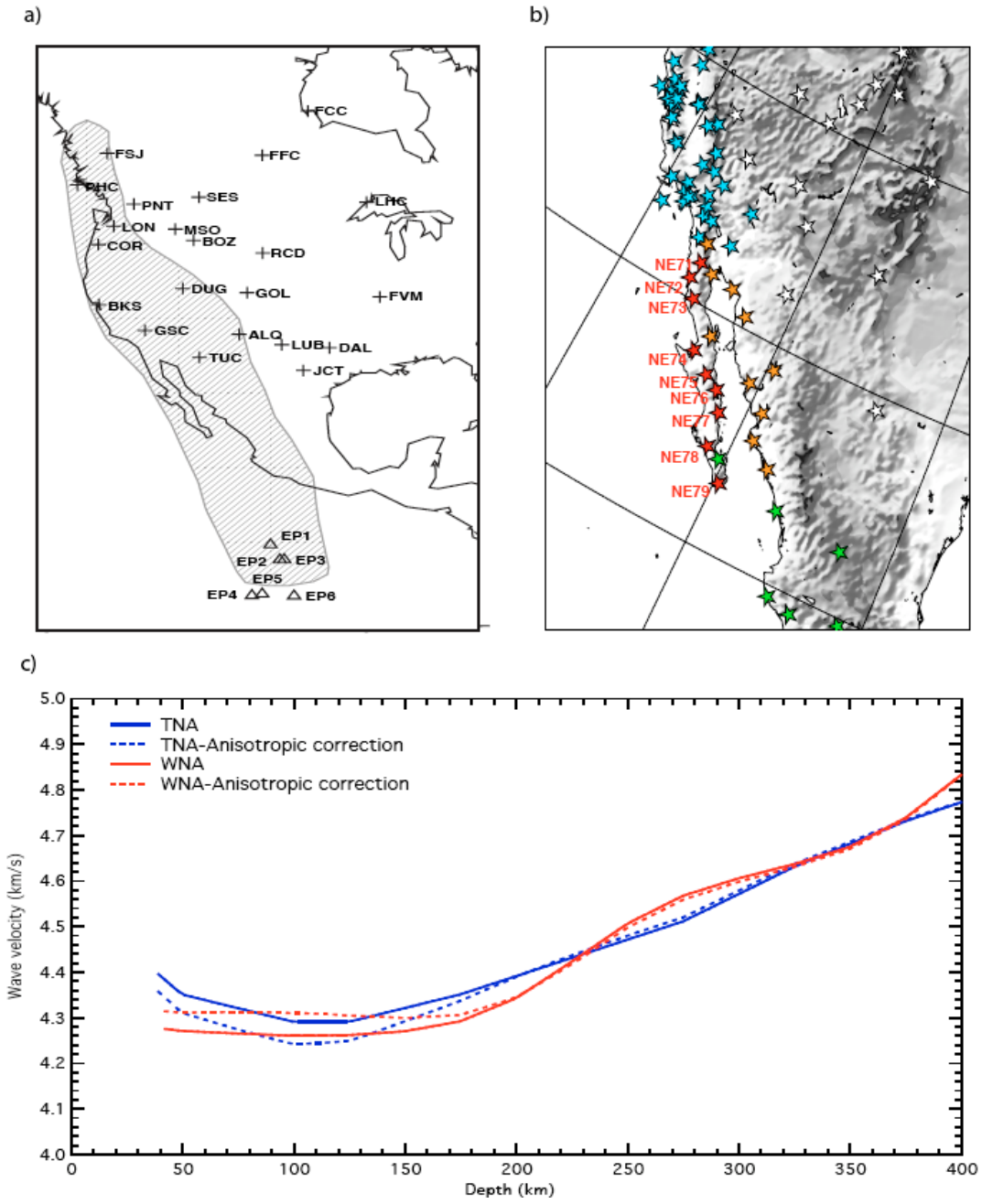

Figure 2.1, a) Maps of events and stations used to construct model TNA. The shaded area is approximately the region of validity for the model (Grand and Helmberger, 1984); b) Events used to construct model WNA (Merrier et al., 2007); c) Solid lines represented TNA (blue) and WNA (red). Dashed line shows the seismic structure after anisotropic correction.

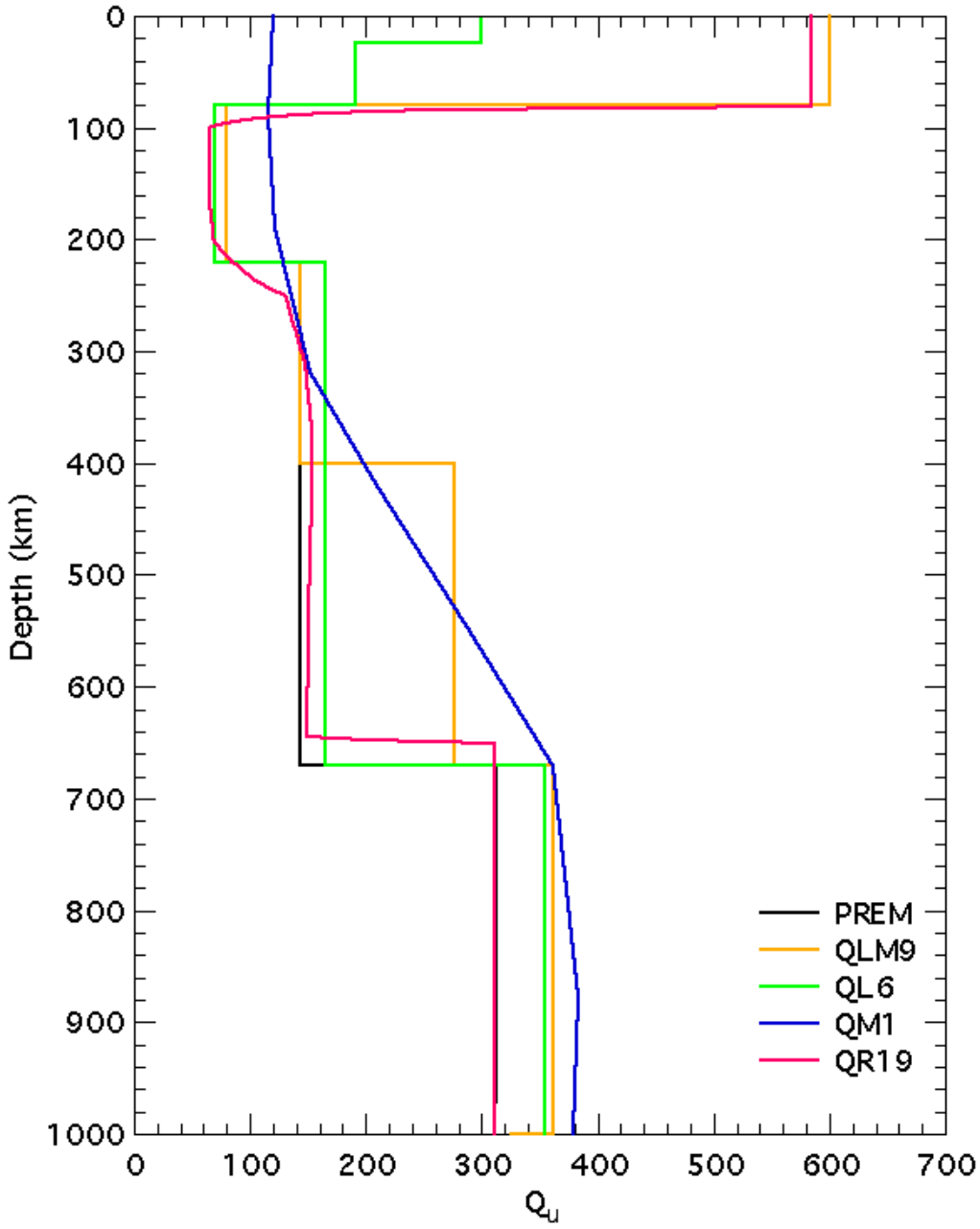

Figure 2.2 Radial models of Q in the mantle. PREM (Dziewonski and Anderson, 1981); QLM9 (Lawrence and Wysession, 2006); QL6 (Durek and Ekstrom, 1996); QM1 (Widmer et al., 1991); QR19 (Romanowicz, 1995)

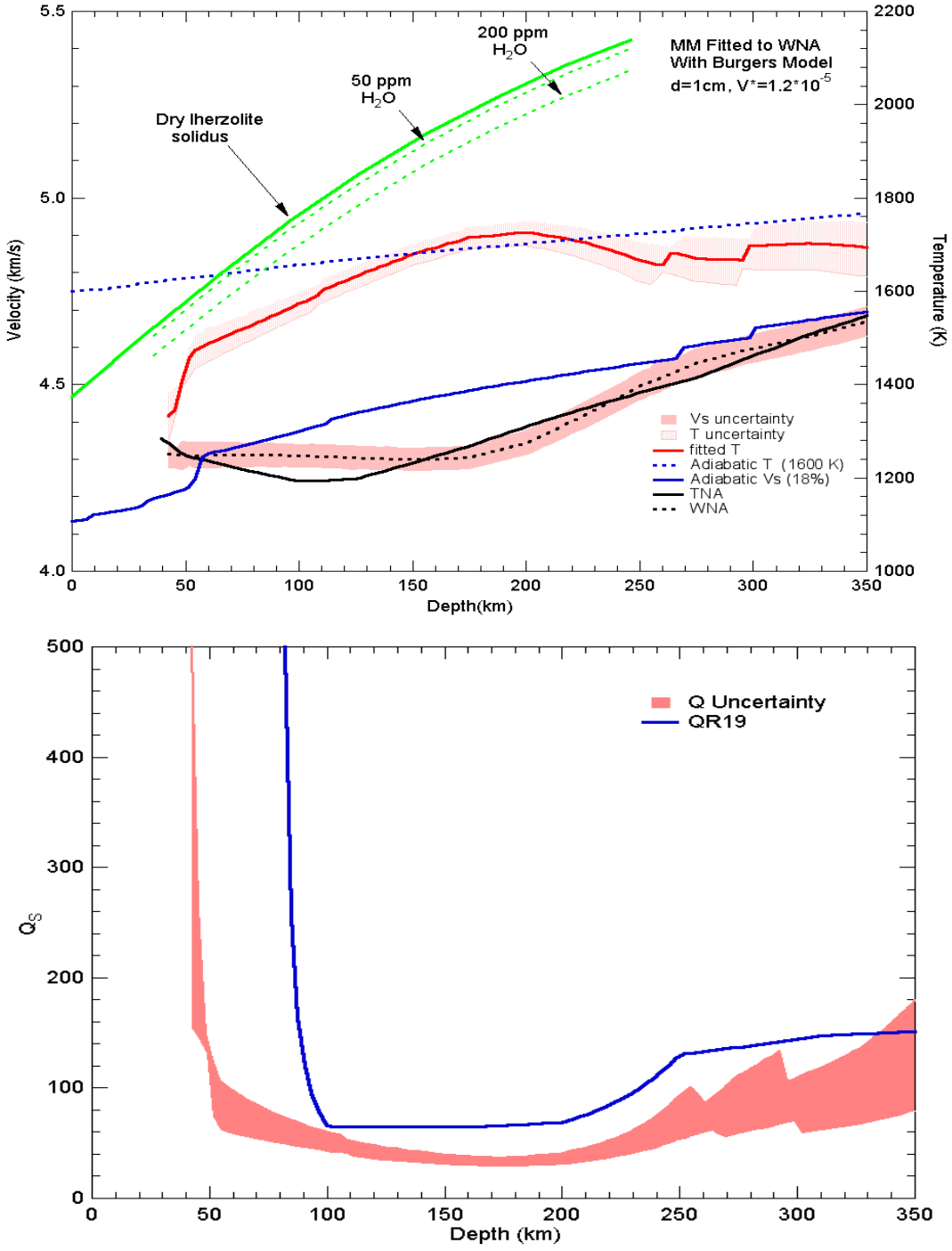

Figure 2.3 Fit to WNA with starting model MM using Q from a Burgers solid model (Faul and Jackson, 2005). Uncertainty of WNA is taken from Merrer et al. (2007). Grain size is 10 mm, activation volume is $1.2*10^{-5}$ m^3mol^{-1}. Other parameters follow table 2.1. Basalt fraction (18%) is fixed through upper mantle. Top is inverted geotherm, and bottom is corresponding Q_S.

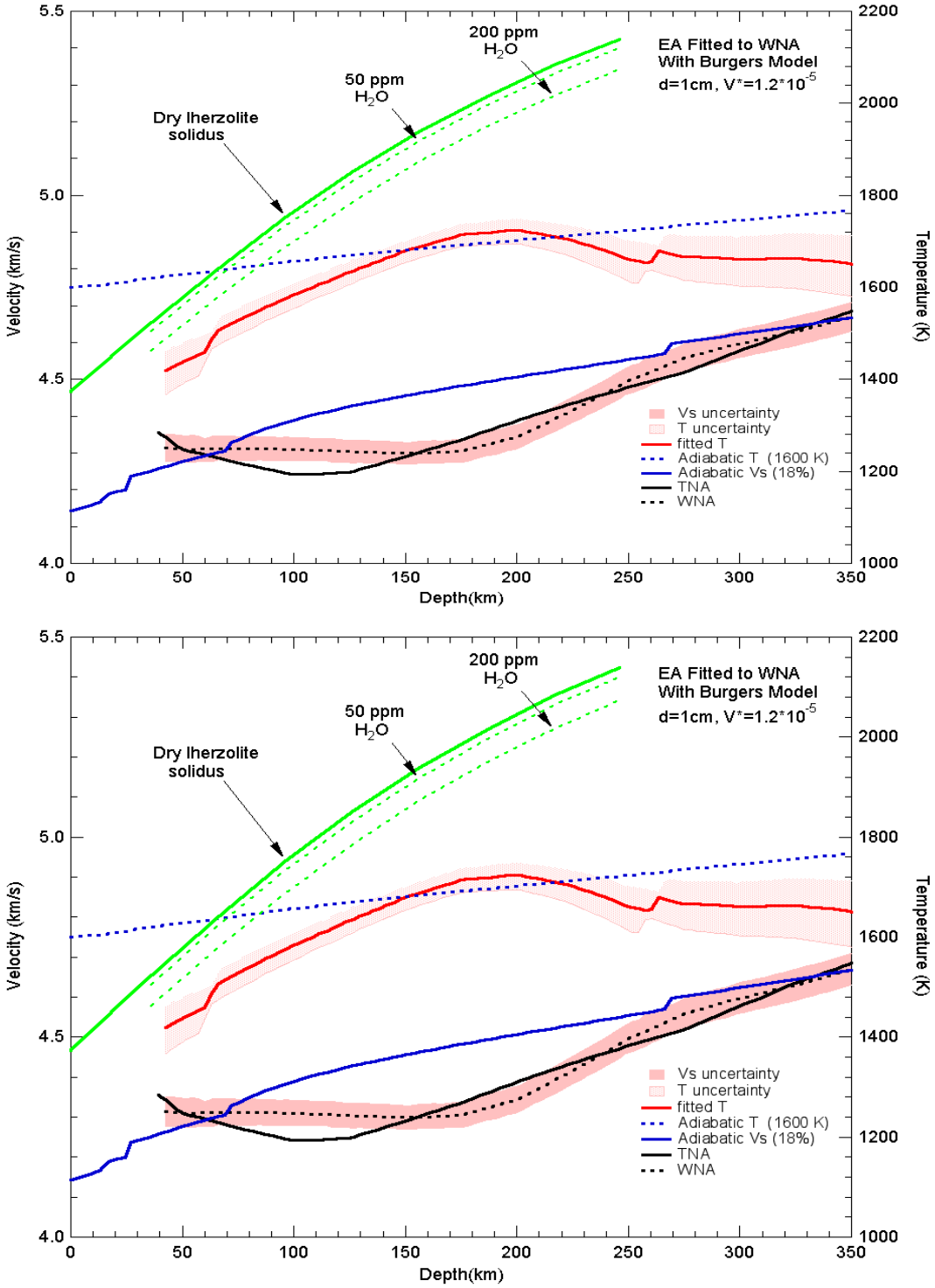

Figure 2.4, same as figure 2.3, but using EA as the starting compositional model. All parameters are identical to the previous figure. EA and MM have identical bulk composition (18% basalt fraction).

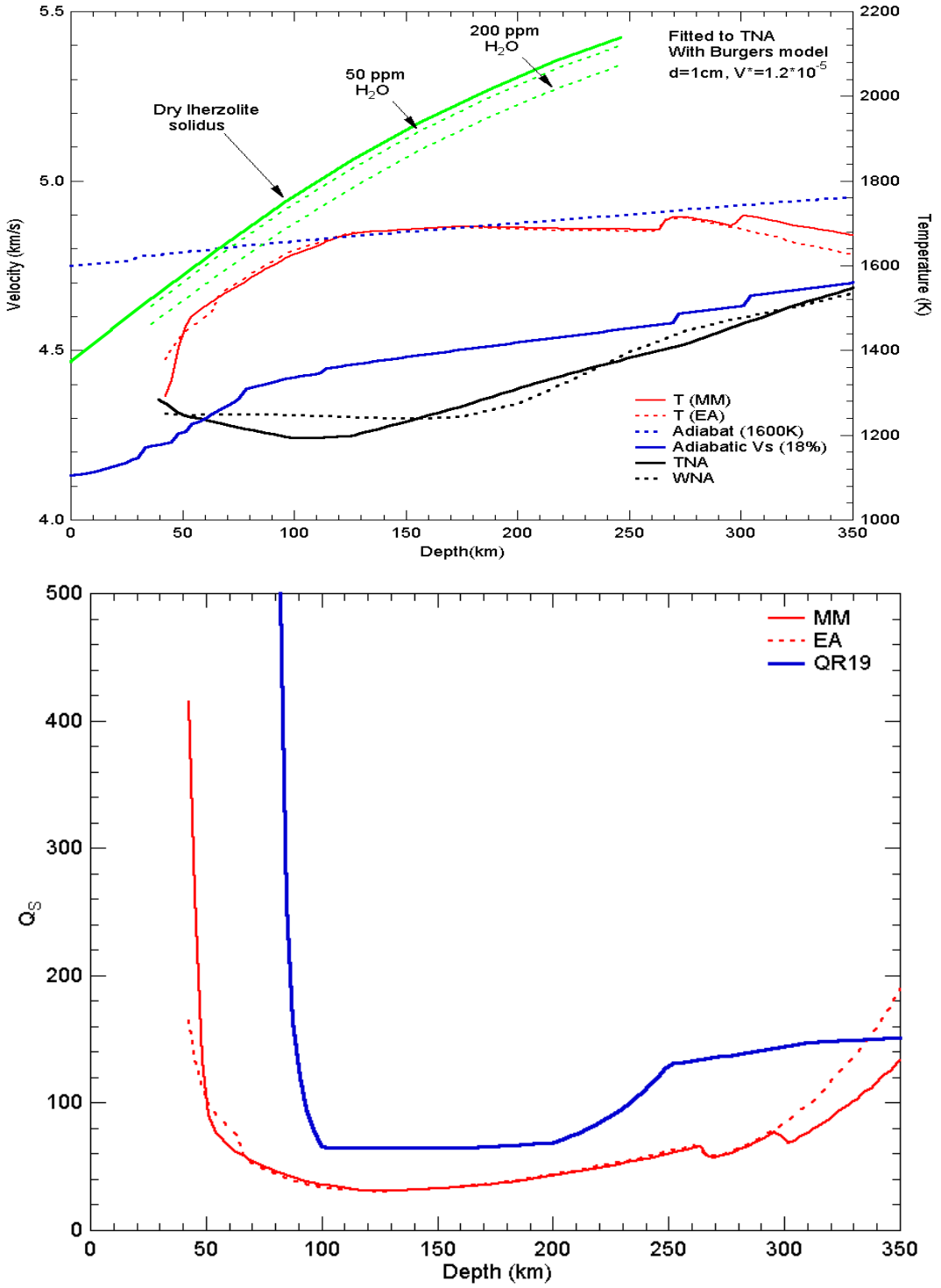

Figure 2.5, Fits to TNA with MM (solid red line) and EA (dashed red line) using the Burgers model. Same parameters are used as in Figure 2.3

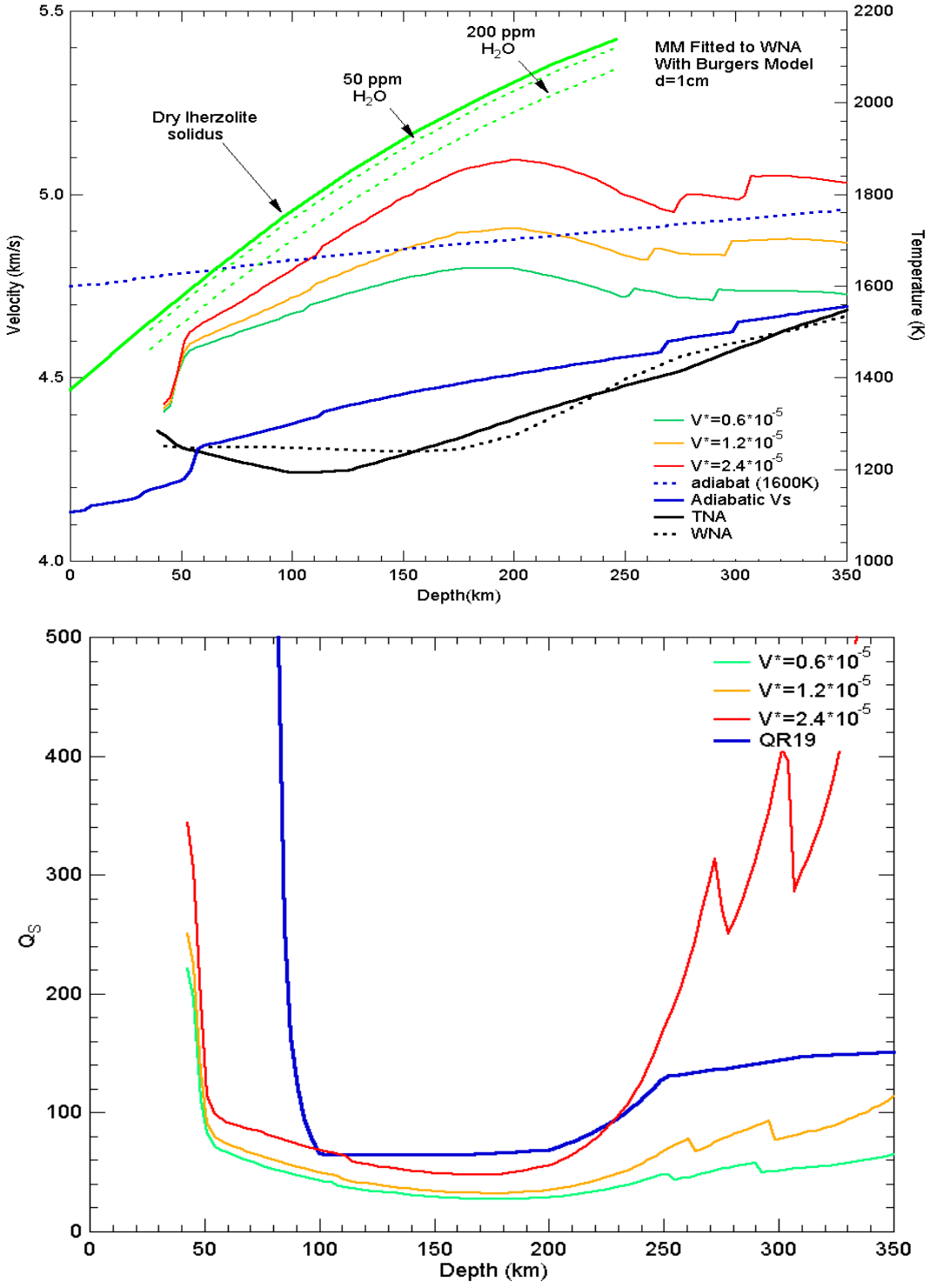

Figure 2.6, Effects of activation volume on inversion. Fits to WNA using MM as the starting compositional (18% basalt fraction) and the Burgers model for Q. Grain size is fixed to be 10 mm. Activation volume of $0.6*10^{-5}$ m^3mol^{-1} (green), $1.2*10^{-5}$ m^3mol^{-1} (orange), $2.4*10^{-5}$ m^3mol^{-1} (red) are explored.

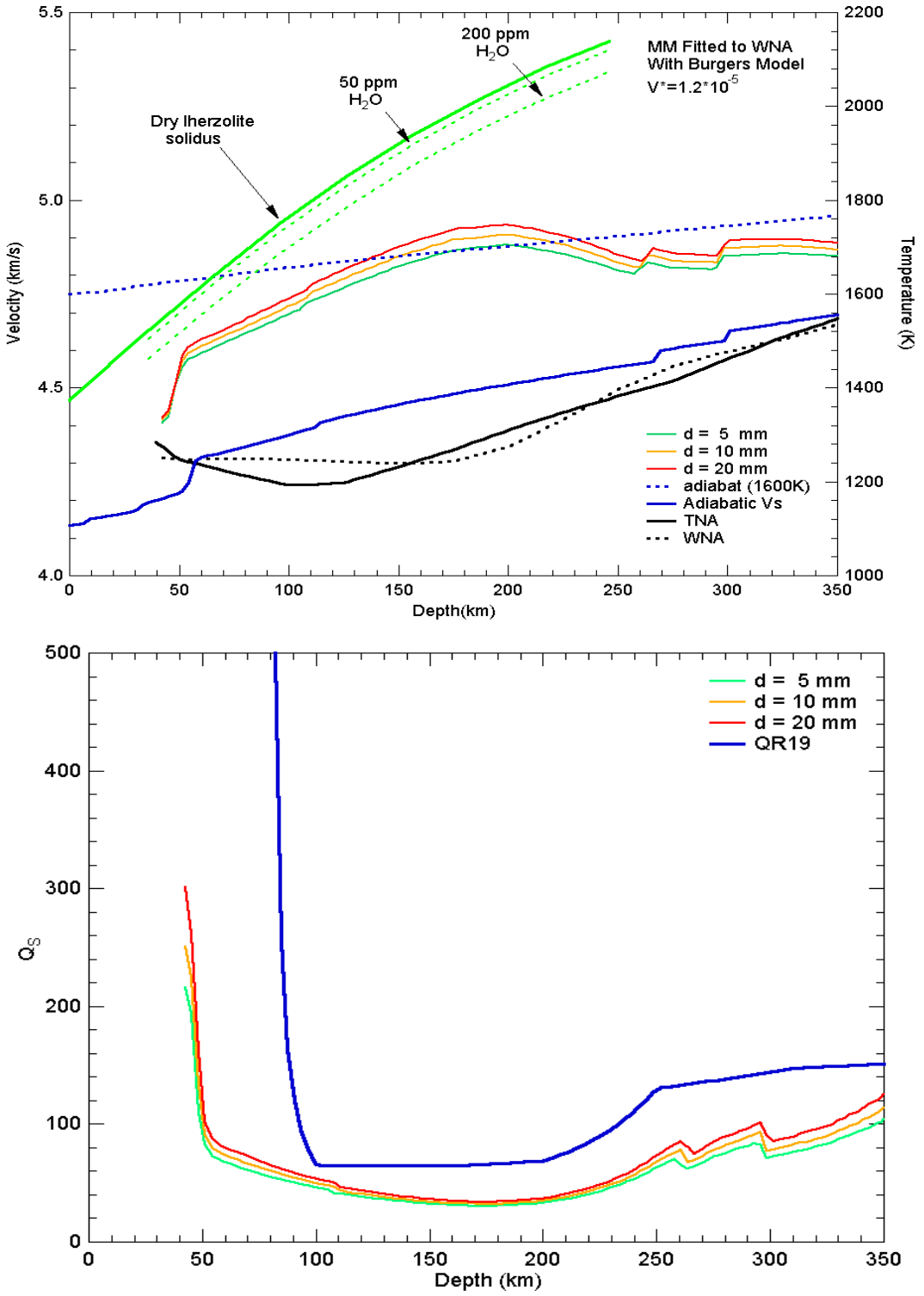

Figure 2.7, Effects of grain size on temperature structure. Fits to WNA using MM as starting compositional model and Q based on a Burgers solid. Activation volume is fixed to be $1.2*10^{-5}$ m^3mol^{-1}. Grain size of 5 mm (green), 10 mm (orange), 20 mm (red) are shown.

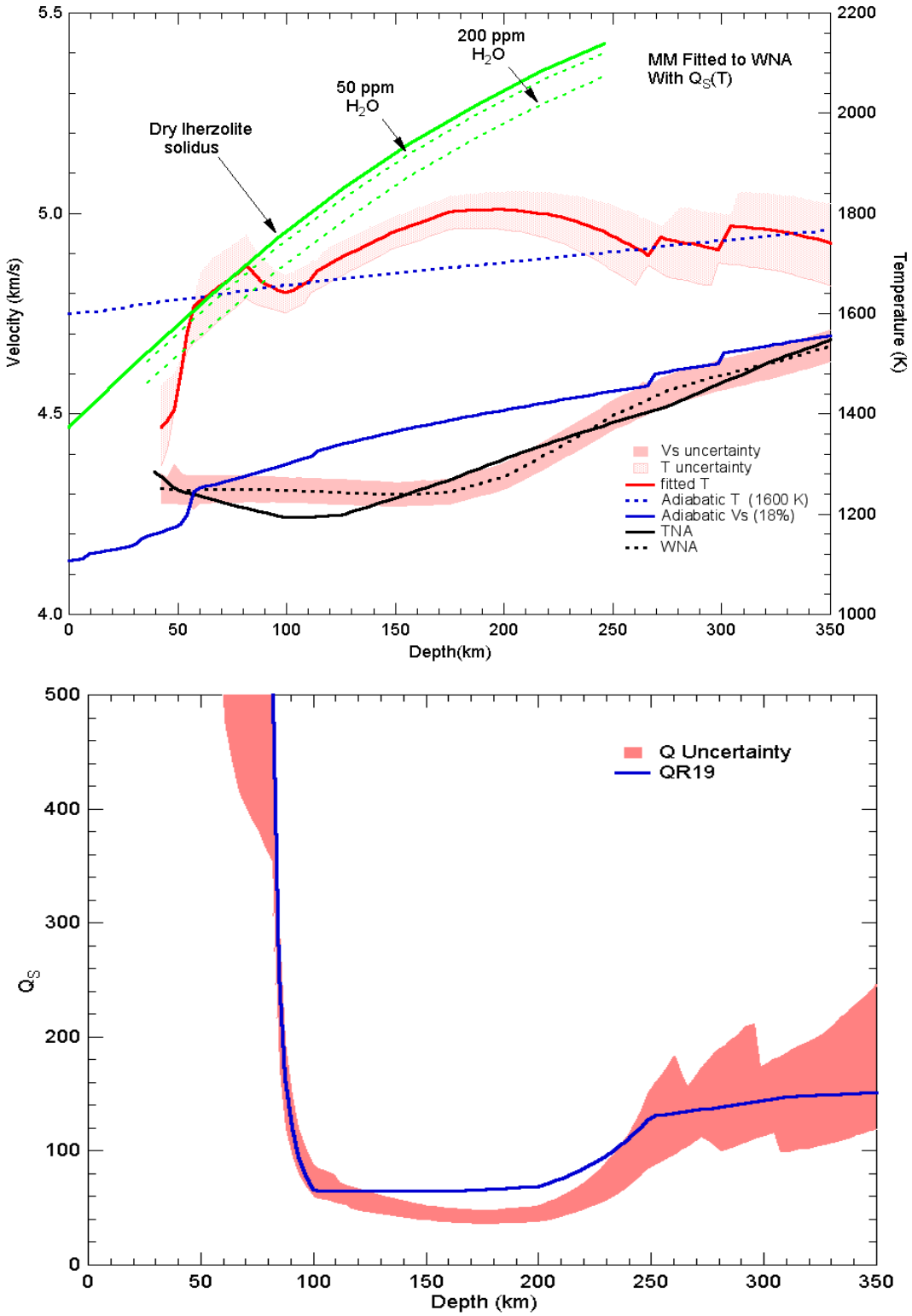

Figure 2.8 Inverted geotherms for WNA starting from MM and Q(T) based on QR19. The reference temperature is the 1600 K adiabat.

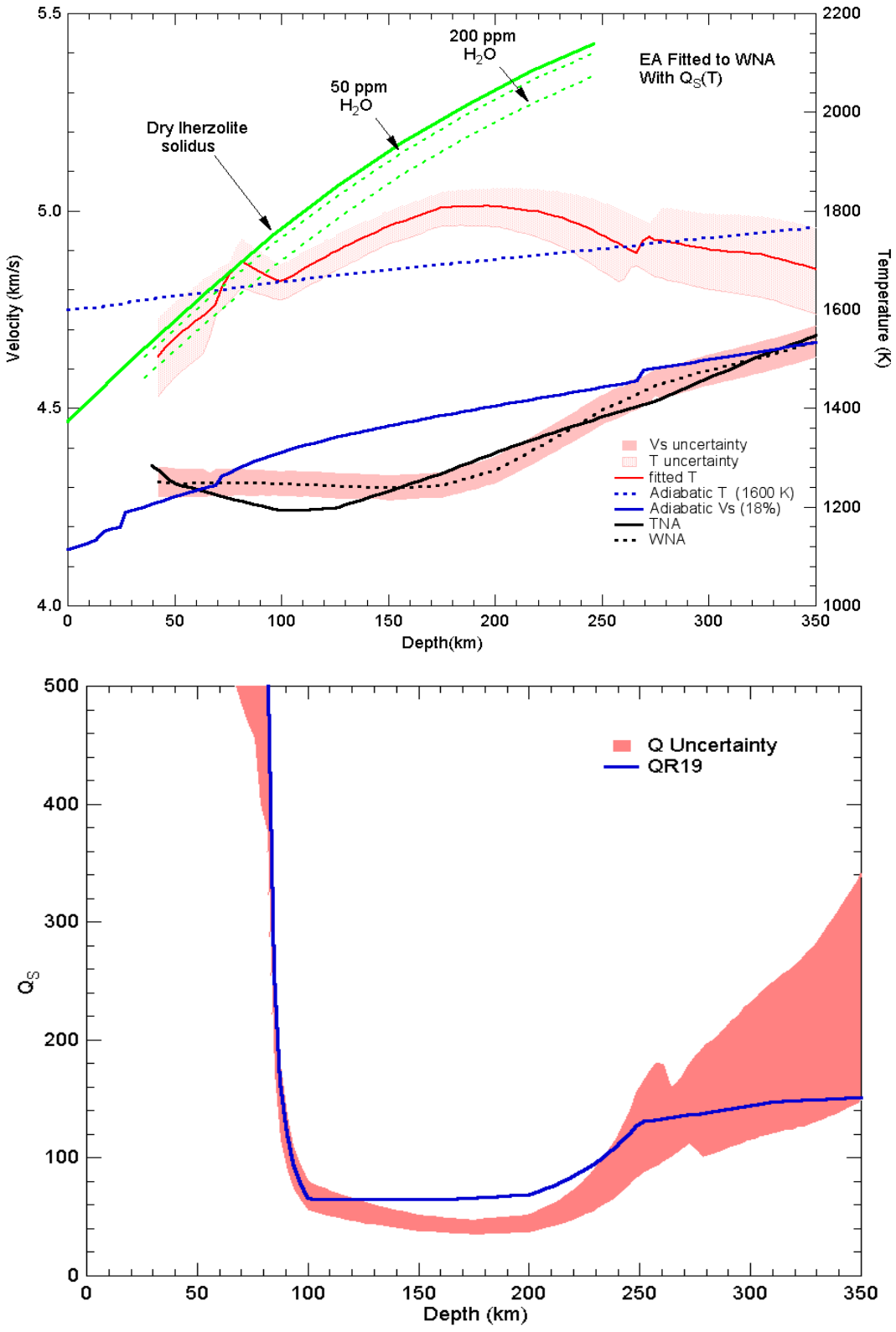

Figure 2.9, same as figure 2.8, but using EA as the fitting model.

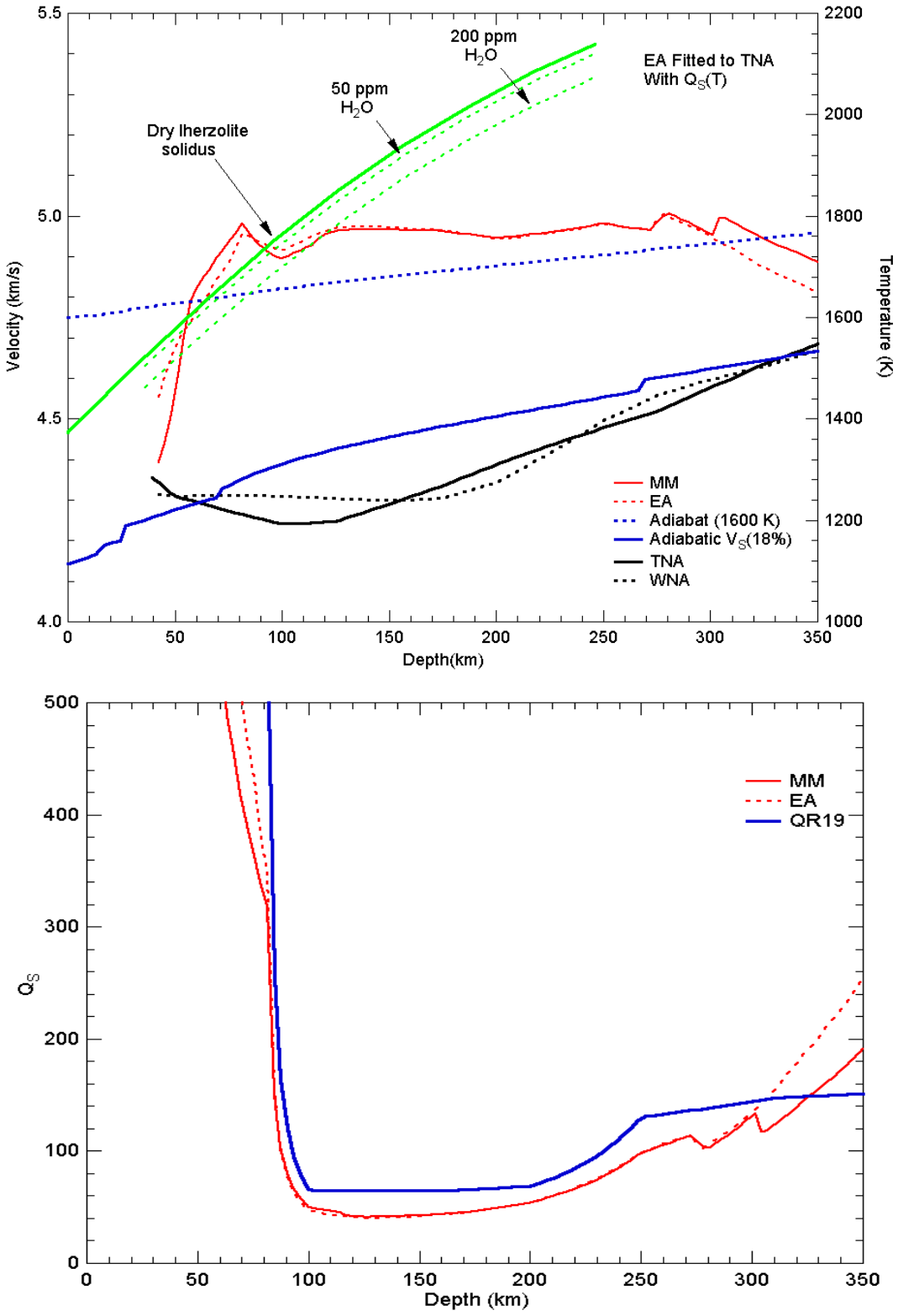

Figure 2.10, Temperature profiles inverted from fitting to TNA for both MM (red solid line) and EA (red dashed line) compositional models.

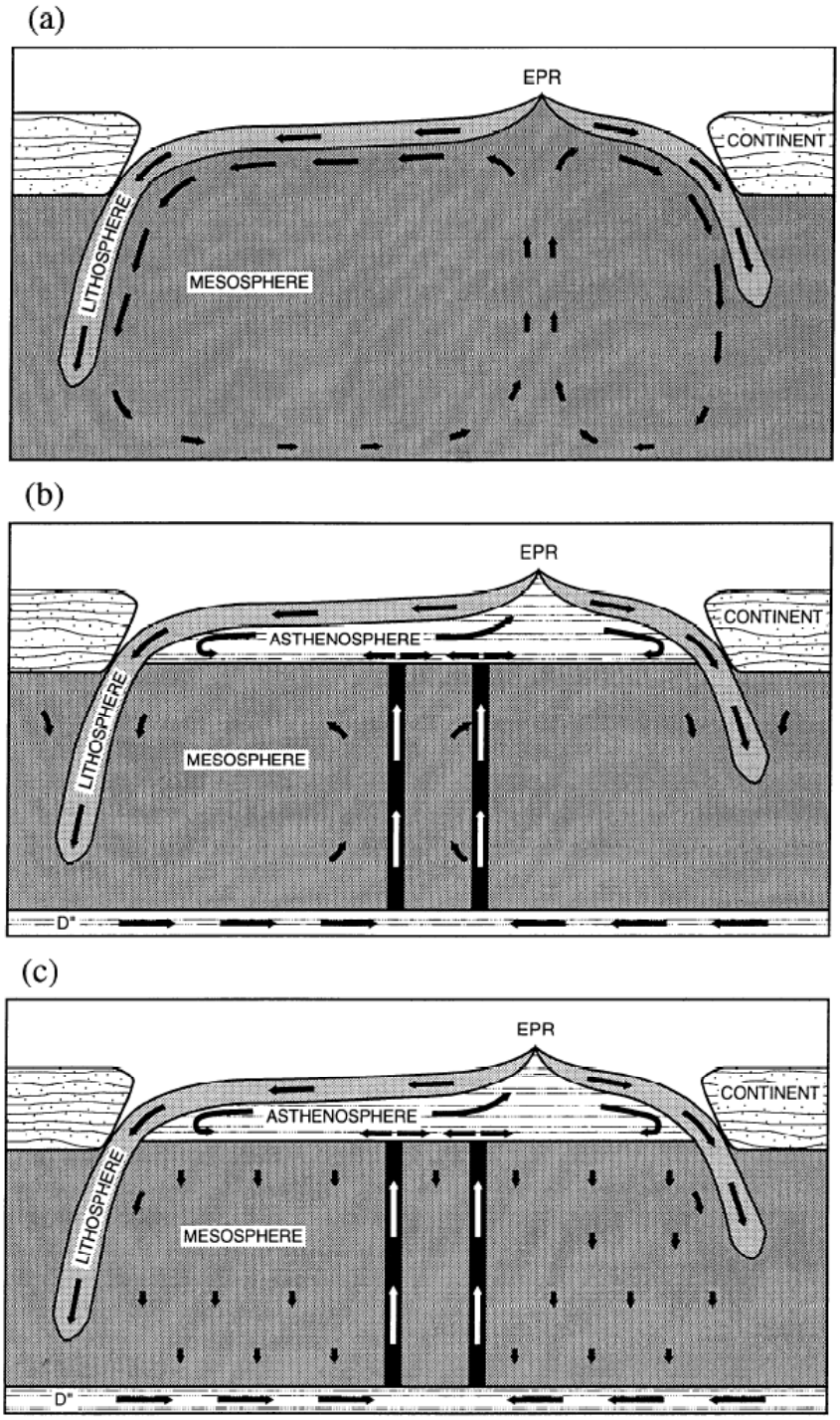

Figure 2.11, plumeyard cartoon. a) surface plate motions are part of a single mantle flow circulation; b) suboceanic asthenosphere layer acts to decouple surface plate motions from deeper mantle flow. The weak asthenosphere layer is preferentially fed by the upwelling plumes from the lower mantle; c) net mantle motion is downward except in areas of plume upwelling . From Morgan et al. (1995)

2.5 References

Anderson, D.L., and Archambeau, C.B., 1966. The anelasticity of the Earth. J. Geophys. Res., 69, 2071-2084

Anderson, D.L., and Sammis, C., 1969. The low velocity zone, Geofis. Int., 9, 3-19

Baker, M.B., Beckett, J.R., 1999. The origin of abyssal peridotites: a reinterpretation of constraints based on primary bulk compositions. Earth Planet. Sci. Lett. 171, 49-61.

Buland, R., and Gilbert, F., 1978. Improved resolution of complex eigenfrequencies in analytically continued seismic spectra. Geophys. J.R. astr.
Soc. Volume 52, Issue 3, pp 457-470

Callen, H.B., 1960. Thermodynamics. John Wiler & Sons, New York.

Chan, W.W., and Der, Z.A.,1988, Attenuation of multiple ScS in various parts of the world. Geophys. J. Int., 92(2), 303–314 doi:10.1111/j.1365-246X.1988.tb01141.x

Davies, G.F. 1988. Ocean bathymetry and mantel convection, 1, large-scale flow and hotspots, J.Geophys. Res., 93, 10,467-10,480

Deschamps, A., 1977. Inversion of the attenuation data of free oscillations of the Earth (fundamental and first higher modes). Geophys. J. R. astr. Soc. Vol. 50 Issue 3 P 699-722

Dziewonski, A. M., and Anderson, D. L.,1981. Preliminary reference earth model. Phys. Earth Planet. Inter., 25, 297-356.

Durek, J. J. and Ekstrom, G., 1996. A radial model of anelasticity consistent with long-period surface wave attenuation. Bull. Seism. Soc. Am., Vol. 86, No. 1A. pp. 144-158

Flanagan, M.P. and Wiens, D.A., 1990. ttenuation structure beneath the Lau back arc spreading center from teleseismic S phases. Geophys. Res. Lett., VOL. 17, NO. 12, P. 2117–2120

Forsyth, D.W., 1999. Geophysical constraints on mantle flow and melt generation beneath mid-ocean ridges, Mantle Flow and Melt Generation at Mid-Ocean Ridges, Geophysical Monograph, vol. 71, American Geophysical Union, Washington, USA, pp. 1-65

Fual, U.H., and Jackson, I., 2005, The seismological signature of temperature and grain size variations in the upper mantle, Earth Plant. Sci. Lett., 234, 119-134

Gilbert, F., and Dziewonski, A.M., 1975. An Application of Normal Mode Theory to the Retrieval of Structural Parameters and Source Mechanisms from Seismic Spectra. Philosophical Transactions of the Royal Society of London. Series A, Mathematical and Physical Sciences, Vol. 278, No. 1280 (Mar. 20, 1975), pp. 187-269

Grand, S.P., Helmberger, D.V., 1984. Upper Mantle shear Structure of North America. Geophys. J.R. astr. Soc. 76, 399-348

Green, D.H., and Liebermann, R.C., 1976, Phase-equilibria and elastic properties of a pyrolite model for oceanic upper mantle,Tectonophysics,32,61–92.

Gribb, T. T., and Cooper, R.F., 1998. Low-frequency shear attenuation in polycrystalline olivine: Grain boundary diffusion and the physical significance of the Andrade model for viscoelastic rheology, J. Geophys. Res., 103, 27,267-27,279

Gutenberg, B., 1959, Physics of the Earth's interior, Springer, New York

Hirth, G. and Kohlstedt, D., 2003. Rheology of the upper mantle and the mantle wedge: a view from experimentalists, Inside the Subduction Factory, Geophys. Monogr., vol. 138, 2003, pp. 83 – 105.

Jackson, I., Paterson, M.S. and Fitz Gerald, J.D., 1992, Seismic wave attenuation in Aheim dunite: An experimental study, Geophys. J. Int., 108,517-534

Jackson, I., Fitz Gerald, J.D., Faul, U.H., et al., 2002. Grain-size-sensitive seismic wave attenuation in polycrystalline olivine. J.Geophys. Res., Vol. 107, No. B12, 2360, doi:10.1029/2001JB001225

Jobert, N. and Roult, G., 1976. Periods and damping of free oscillations observed in France after sixteen earthquakes, Geophys. J. R. Astr. Soc. 45, 155-176.

Kanamori, H., 1970. Velocity and Q of mantle waves. Phys. Earth Plant. Interiors 2, 259-275

Kovack, R. L., and Anderson, D.L., 1964. Attenuation of shear waves in the upper and lower mantle. Bull. of the Seism. Soc. of Am. v. 54; no. 6A, p. 1855-1864

Lambert, I. B., and P.J. Wylllie, 1968. Stability of hornblende and a model for low velocity zone, Nature, 219, 1240-1241

Lay, T., and Wallace, T. C., 1983. Multiple SCS travel times and attenuation beneath Mexico and Central America. Geophys. Res. Lett., Volume 10, Issue 4, p. 301-304

Merrer, S., Cara, M., Rivera, L., et al., 2007. Upper mantle structure beneath continents: New constraints from multi-mode Rayleigh wave data in western North American and south Africa. Geo. Res. Lett., Vol. 34, L06309, doi:10.1029/2006GL028939.

Morgan, J.P., Morgan, W.J. and Zhang Y., 1995. Observational hints for a plume-fed, suboceanic asthensphere and its role in mantle convection. J. Geophys. Res. 100, pp012753-12767

Nishimura, C.E., and Forsyth, D.W. 1989. The anisotropic structure of the upper mantle in the Pacific. Geophys. J. Int., 96, 203-229

Nakanishi, I., 1979. Phase velocity and Q of mantle Rayleigh waves. Geophys. J.R. astr. Soc. Volume 58, Issue 1, pp 35-59

Richards, M. A., Yang W., Baumgardner J. R., et al., 2001. Role of a low-viscosity zone in stabilizing plate tectonics: implications for comparative terrestrial planetology. Geothem. Geophys. Geosyst., 2, doi:10.1029/2000GC000115

Ringwood, A. E., 1969. Composition and evolution of the upper mantle, in The Earth's Crust and Upper Mantle: Structure, Dynamic Processes, and Their Relation to Deep-Seated Geological Phenomena, Geophys. Monogr. ser., Vol. 13, editeb by P.J. Hart, pp. 1-17, AGU, Washington, D. C.

Romanowicz, B., 1995. A global tomographic model of shear attenuation in the upper mantle. J. Geophys. Res. Vol. 100, No. B7, 12,375-12394

Romanowicz, B., and Durek, J.J., 2000. Seismological constraints on attenuation in the earth: a review: in Karato, S., Forte, A., Liebermann, R., Masters, G., Stixrude, L., (Eds.) Earth's Deep Interior:Mineral Physics and Tomography from atomic to the global scale. AGU Geophysical Monograph, 117, 265-289

Roult, G., 1975. Attenuation of seismic waves of very low frequency. Phys. Earth Planet. Interiors, Volume 10, Issue 2, p. 159-166

Sailor, R.V. and Dziewonski, A.M., 1978. Measurements and interpretation of normal mode attenuation, Geophys. J. R. astr. Soc., 53, 559-581

Sato, H., Sacks, I. S., and Murase, T., 1989. The use of laboratory velocity data for estimating temperature and partial melt fraction in the low-velocity zone: Comparison with heat flow and electrical conductivity studies, J. Geophys. Res., 94, 5689–5704.

Sikpin, S. A., and Jordan, T.H., 1980. Regional variation of Q_{ScS}. Bull. of the Seism. Soc. of Am., v. 70; no. 4; p. 1071-1102

Stein, S., and Geller, R.J., 1978. Attenuation measurements of split normal modes for the 1960 Chilean and 1964 Alaskan earthquakes. Bull. of the Seism. Soc. of Am., v. 68; no. 6, p. 1595-1611

Stixrude, L., Lithgow-Bertelloni, C., 2005a. Mineralogy and elasticity of oceanic upper mantle: Origin of the low velocity zone. J Geophys. Res. 110, B03204, doi:10.1029/2004JB002965

Stixrude, L., and Lithgow-Bertelloni, C., 2005b. Thermodynamics of mantle minerals – I. Physical properties. Geophys. J. Int., Volume 162 Issue 2 Page 610-632, doi:10.1111/j.1365-246X.2005.02642.x

Tackley, P., 2000. Self-Consistent generation of tectonics plates in time-dependent, three-dimensional mantle convection simulations, Part 2: Strain weakening and Asthenosphere. Geothem. Geophys. Geosyst. (2000GG000036)

Tan, B.H., Jackson, I., and Fitz Gerald, J.D., 1997. Shear wave dispersion and attenution in fine-grained synthetic olivine aggregates: Preliminary results, Geophys. Res. Lett., 24,4055-1058

Tan, B.H., Jackson, I., and Fitz Gerald, J.D., 2001. High-temperature viscoelasticity of fine-grained polycrystalline olivine, Phys. Chem. Miner., 28, 641-664

Watt, J. P., Davies, G. F., and O'Connell, R. J., 1976. The elastic properties of composite materials. Rev. Geophys. Space Phys. 14, 541-563

Widmer, R., Matsters, G., and Gilbert, F., 1991. Spherically symmetric attenuation within the earth from normal mode data, Geophys. J. Int., 104, 541-553

Workman, R.K., Hart, S. R., 2005. Major and trace element composition of the depleted MORB mantle (DMM). Earth Planet. Sci. Lett. 231, 53-72.

Xu, W., Lithgow-Bertelloni, C., Stixrude, L., and Ritsema, L., 2008. The Effect of Bulk Composition and Temperature on Mantle Seismic Structure. Earth Plant. Sci Lett., Submitted

Yoshida, M. and M. Tsujiura, 1975. Spectrum and attenuation of multiply reflected core phases, J. Phys. Earth 23, 31-42.

Chapter III
The role of the transition zone in mantle convection

3.1 Introduction

The pattern of mantle convection below the upper thermal boundary layer has important consequences for our understanding of Earth's thermal and chemical evolution. Vigorous debate about whether the mantle convects in a single layer from surface to core (Davies, 1977; O'Connell, 1977; Peltier, 1976; Schubert, 1979), or whether upper and lower mantle convect separately (Allégre et al., 1980; Allégre et al., 1996; De Paolo & Wasserburg, 1976; Jacobsen & Wasserburg, 1979; O'Nions et al., 1979; Ritchter and Johnson, 1974; Schubert et al., 1975; Turner, 1989; Turekian, 1959) has now given way to a more complex picture. Seismic tomography demonstrates mass flux across the upper mantle-lower mantle boundary (Bijwaard et al., 1998; Fukao et al., 1992; Fukao et al., 2001; Grand 1994; Karason and van der Hilst, 2000; van der Hilst et al., 1991; van der Hilst et al., 1997; Zhou and Clayton 1990). At the same time, tomographic images also show that the descent of at least some subducting slabs its impeded by the upper mantle-lower mantle boundary (Flanagan and Shearer 1998; Giardini and Woodhouse 1984; Grand et al., 1997; Knopoff 1964; Lundgren and Giardini 1994; Okino et al., 1989; Richards and Wicks 1990; van der Hilst et al., 1997). Evidence from mantle isotope and trace element geochemistry for deep primordial reservoirs (Allégre et al., 1996; Anderson, 1981; De paolo, 1981; Jacobsen and Wasserburg, 1979; O'Nions et al., 1979; Turekian 1959; Turner 1989; Wasserburg and De Paolo, 1979) demands long-lived

chemical heterogeneity in the mantle, but with few constraints on the geometry of contrasting reservoirs.

The key to understanding the nature of mantle convection lies in the transition zone between upper and lower mantles. This is the region in which subducting slabs appear to accumulate (Christensen, 1995; Honda et al., 1993; Machetel and Weber 1991; Solheim and Peltier 1994; Tackley et al., 1993; Weinstein et al., 1993). Moreover, one expects on theoretical grounds that phase transitions at the bottom of this region will impede mass flux between upper and lower mantle (Davies 1988 a, b; Hager 1984; Nakagawa and Buffet, 2004; Tackley 2000; Tackley et al., 1994; Xie and Tackley, 2004).

The structure of the transition zone is anomalous. The deviation of the Bullen inhomogeneity parameter (Bullen, 1963) from unity demonstrates that the transition zone is either inhomogeneous in composition, or phase, or has a non-adiabatic temperature profile, or some combination of all three (Bunge et al., 1997; Bunge et al., 2001; Heinz and Jeanloz, 1983; Matyska and Yuen, 2000,2002; Parmentier et al. ,1994; Tackley et al., 1994). The transition zone has an anomalously high velocity gradient: S- and P-wave velocities increase much more rapidly with increasing depth than in the sub-lithospheric upper-mantle or in the lower-mantle. Phase transitions are almost certainly present, based on evidence from experimental mineral physics, and the analysis of xenoliths. Recent analyses indicate that these phase transitions, while having the effect of increasing the velocity gradient, are insufficient by themselves to explain it (Xu et al., 2008).

Here we investigate the origin of transition zone structure, and test the hypothesis that, in addition to being inhomogeneous in phase, this region may also be radially inhomogeneous in chemical composition, or entropy, i.e. whether the temperature is non-

adiabatic. Our approach goes beyond previous analyses as it is based on a self-consistent thermodynamic description of the phase equilibria and physical properties of this region, as opposed to previous non self-consistent treatments. We compare the P- and S-wave velocities computed from this method to seismological models of the transition zone, and perform inversions to find the radial temperature structure that best matches the seismological models for a range of bulk chemical compositions.

3.2 Methodology

Our analysis is based on the self-consistent thermodynamic method of Stixrude and Lithgow-Bertelloni (2005a; 2005b) described in Chapter 1. Given pressure, temperature, and bulk chemical composition, this method yields phase proportions, phase compositions, and physical properties of individual phases and of the bulk rock, including P- and S-wave velocities in the elastic limit and the entropy.

We explore a range of bulk compositions, defined by the basalt fraction, as in our previous work (Chapter 1), including models that are fully equilibrated (equilibrium assemblage: EA) and models in which basalt and harzburgite fractions are un-equilibrated (mechanical mixture: MM).

The effect of attenuation and dispersion is included via the finite shear quality factor

$$Q(z) = Q_{00}(z) \exp\left[\frac{\alpha E^*}{R}\left(\frac{1}{T(z)} - \frac{1}{T_R(z)}\right)\right] \tag{3.1}$$

where $Q_{00}(z)$ is the radial part of the seismological quality model QR19 (Romanowicz, 1995), T is the temperature, T_R is the temperature along the 1600 K adiabat, and values of the activation energy E*= 424 kJ mol^{-1} K^{-1} and frequency exponent, ⟨=0.26, are from Jackson et al. (2002). The activation energy is assumed to be independent of pressure in the absence of experimental data at elevated pressure. Allowing E* to depend on pressure via the Weertman law, or a plausible finite value of the activation volume, has little influence on the results of our study.

We perform the inversion for temperature structure as follows. At each depth, z, we find the value of the temperature T_S such that

$$V_S^{thermo}(X,z,T_S) - V_S^{seismo}(z) = 0 \qquad (3.2)$$

where V_S^{thermo} is the shear wave velocity computed from our model for a given bulk composition X and V_S^{seismo} is the velocity of the seismological model, As seismological models differ depending on the data used, the inversion formalism, and modeling assumptions (i.e. parameterization), we examine two different seismological models (figure 3.1): PREM (Dziewonski and Anderson, 1981), which is a global model of V_S, V_P and density, based on body-waves and normal modes, and TNA (Grand and Helmburger, 1984), which is a regional V_S model of western North America based on body and surface waves.

3.3 Results

3.3.1 Global Model-PREM

Figure 3.2 shows the result of inverting the shear wave velocity of PREM with EA. The inverted temperature lies below the 1600 K adiabat everywhere in the transition zone,

except in the immediate vicinity of the 410 km discontinuity. Moreover, there is a tendency for the inverted temperature to decrease with increasing depth: at 650 km depth, the inverted temperature is 200 K (MM) (Figure 3.2) to 300 K (EA) (Figure 3.4) colder than the adiabat for a pyrolitic bulk composition. Superimposed on these trends, which are found for all compositions investigated, are large excursions in the inverted temperature in the vicinity of phase transformations. These large excursions arise because features in the velocity structure due to phase transformations either do not have counter-parts in the seismological model (wa=ri near 520 km depth), or because the position of the equilibrium transition occurs at a depth different from that assumed in the seismological model. For example, we find the olivine=wadsleyite transition to occur near 410 km depth on the 1600 K adiabat, whereas PREM places a discontinuity at 400 km depth. Indeed, our positioning of the transition is in better agreement with more recent studies. The datasets that are used to construct global models such as PREM are not very sensitive to the position of discontinuities.

We also compared our computed values of V_P and density along the inverted temperature profile to PREM (Figs. 3.3,3.5). The computed P-wave velocity agrees with the PREM transition zone best for a pyrolite-like composition (18% basalt fraction) within the transition zone. The density does not agree as well, but it must be recognized that this is the part of global models that is least constrained. In particular, the magnitude of the density jumps at 410 km and 660 km assumed in PREM are virtually unconstrained by the data.

3.3.2 Regional Model-TNA

Explain here that TNA is SH and the anisotropic correction you made. The geotherm that best fits TNA (Figs, 3.7, 3.8) is hotter and shows a gradient more nearly adiabatic as compared with the geotherm that best fits PREM. The best fitting temperatures are mostly colder in the transition zone than the 1600 K adiabat, by less than 150 K in the case of MM and a pyrolitic basalt fraction (18%). As in the case of PREM, inverted temperatures are less sensitive to composition in the case of MM as compared with EA.

3.4 Discussion and Conclusions

The inverted temperature profiles are not smooth because the seismological models that we have used assumed a linear velocity gradient in the transition zone that is probably not realistic. This artificial feature of the seismological models, combined with the influence of phase transformations on the velocity-temperature relation (Stixrude et al., 2007), accounts for the local minima and maxima in the inverted temperature profiles. Therefore, we consider the local minima and maxima to be an artifact of the seismological models. We focus instead on the mean temperature and mean temperature gradient across the transition zone, which should be robust features, largely independent of assumptions made in the construction of seismological models.

The sub-adiabatic transition zone geotherm that we find on inverting the global model PREM is consistent with several other lines of evidence. Dynamical models of mantle convection that include the influence of phase transformations at 660 km depth all show a tendency of cold down-welling material to accumulate in the deep transition zone (Davies 1988 a, b; Hager 1984; Tackley 2000; Nakagawa and Buffet, 2004; Tackley et al., 1994; Xie and Tackley, 2004) Slab pile-up in the deep transition zone is also seen in

several regional tomographic studies (Flanagan and Shearer 1998; Grand et al., 1997; Lundgren and Giardini 1994; Okino et al., 1989; Richards and Wicks 1990; van der Hilst et al., 1997). We suggest that slab pile-up is globally significant and has a substantial impact on the horizontally averaged temperature at the base of the mantle, which agrees well with dynamic prediction by Tackley et al. (1993) as shown in figure 3.8.

The inverted subadiabatic geotherm is 150-250 K colder than 1600 K adiabat, and we estimate this cooling to correspond to 25~35% volume fraction of slab accumulating at the base of the transition zone (Figure 3.9). For our inverted geotherm, and using as a baseline a typical slab geotherm, ~150-200 K colder than the 1550 K adiabat, we estimate that the implied slab volume fraction in the transition zone is ~25-35%. We obtain similar results by computing the mass fraction (26.4%) of slabs in the transition zone from a kinematic model (figure 2.10) of where slabs may be in the transition zone based on 120 Myr of a subduction and where slow down at 660 km depth due to an expected viscosity contrast between upper mantle and lower mantle (Lithgow-Bertelloni and Richards, 1998). The dynamical and temperature predictions are in remarkably good agreement. Slab accumulation in both implies that slab accumulation is not only real, having an effect on the temperature structure, but it is also due to the increase in viscosity in the upper mantle seen from dynamical models, and only in minor part due to effects of phase transitions. The latter implies that the Clapeyron slopes of perovskite forming reactions in the olivine and garnet largely cancel each other at cold temperature.

An alternative interpretation of our inversions of PREM is that the deep transition zone is depleted in basalt (Irifune et al., 2008). Harzburgite is substantially faster than basalt in this depth range, so that basalt depletion and cooling have similar effect on the

shear wave velocity. However, basalt depletion leads to inferior agreement with V_P and density profiles. Moreover, the opposite: basalt enrichment of the deep transition zone, is expected on dynamically grounds. The argument, advanced by Irifune and Ringwood (1988) and subsequently found in detailed convection simulations is straightforward: at the base of the transition zone, basalt is substantially less dense than harzburgite because the perovskite forming reaction is delayed to much higher pressure. The basaltic portion of downwellings then tends to accumulate above 660 km preferentially.

The more nearly adiabatic gradient of the temperature profile inverted from TNA is consistent with this picture. The study area of TNA is one region where slab pile-up is not expected, because there has not been a large amount of recent subduction. In this region, we expect on dynamical grounds to find more nearly adiabatic temperatures. The slight difference between the inverted temperature and the 1600 K adiabat may signal that the 1600 K adiabat is not optimally representative of normal mantle free of slab accumulation. Indeed, the adiabat that best accounts for the formation of MORB is uncertain by at least 50 K, due to uncertainties related to olivine fractionation and variability of MORB composition. Our results are then consistent with the heat content of the TNA mantle being identical to that of the MORB mantle.

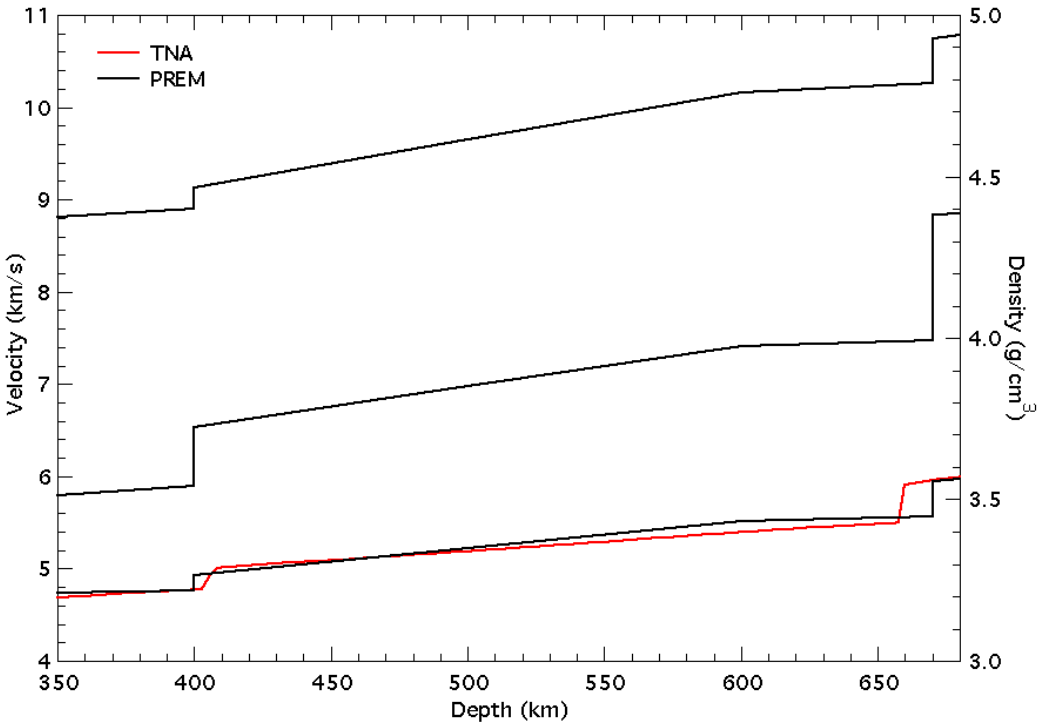

Figure 3.1, Seismic structure of PREM (Dziewonski and Anderson 1981) and TNA (Grand and Helmberger, 1984). TNA is anisotropically corrected by following table 2.2 of Nishimura and Forsyth (1989). However, anisotropy only matters in the upper mantle (above 400 km)

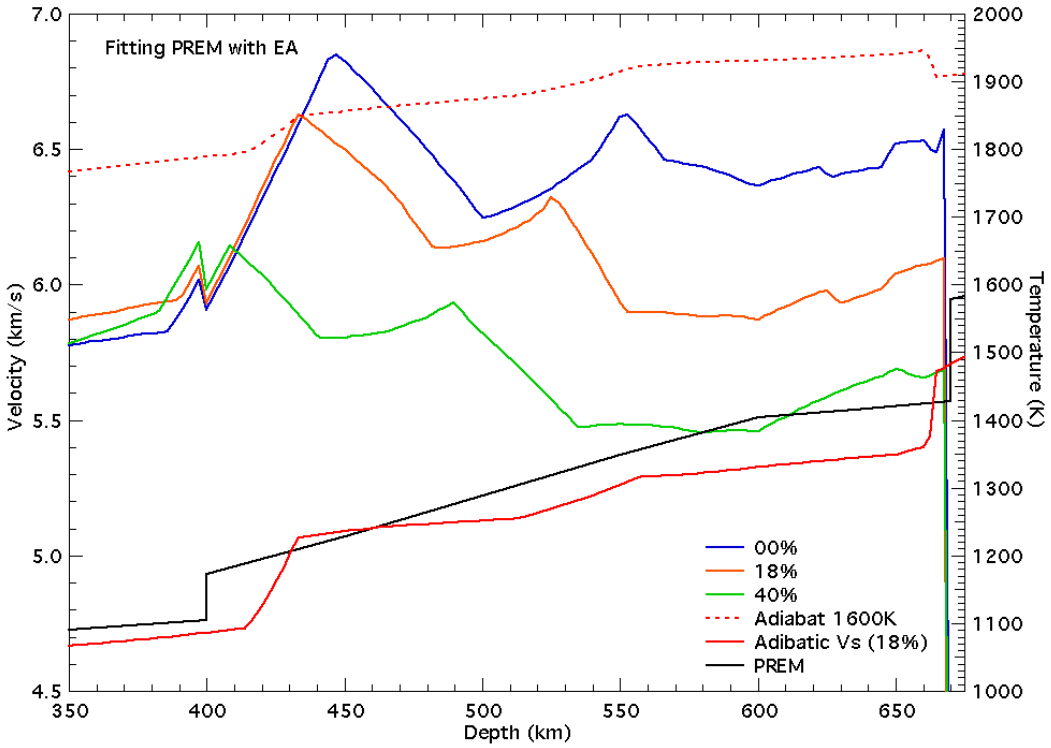

Figure 3.2 Temperature profile that best fits PREM, starting from the EA model for basalt fractions of 0% (blue), 18% (orange), which is the best approximation of basalt fraction in the mantle, and 40%.

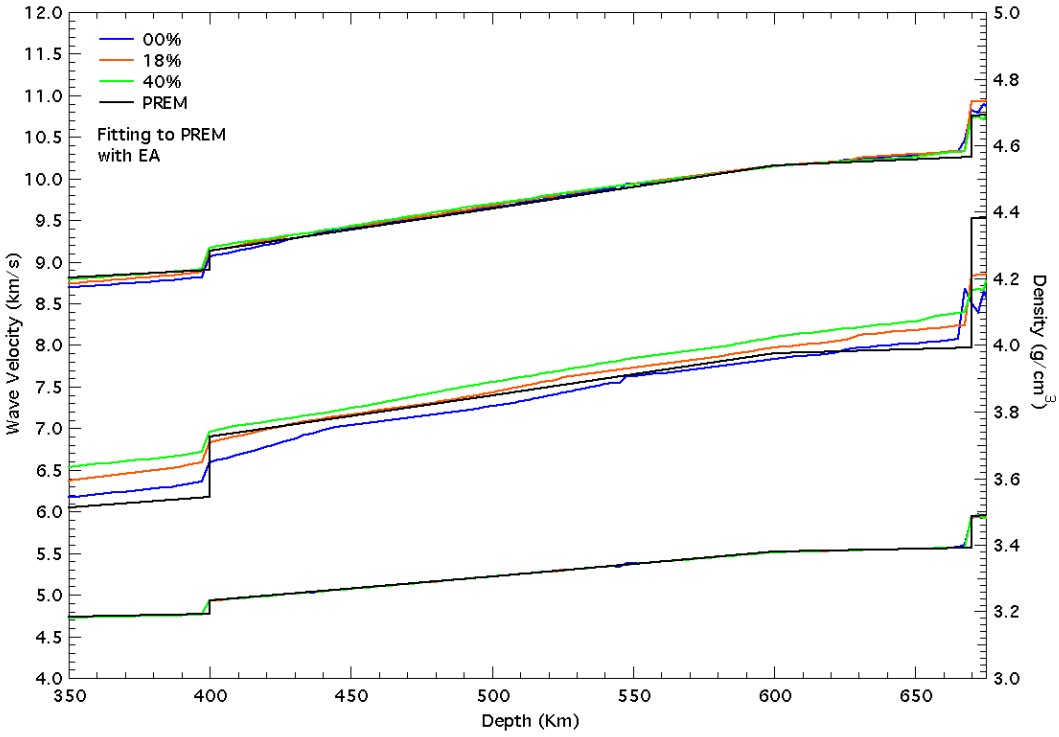

Figure 3.3, V_S fitted to PREM with EA as staring model and basalt fractions as in previous figures. Density and V_P are calculated using the inverted geotherm. V_P and V_S fit pretty well, but not density. It indicates that V_P and V_S are consistent in the transition zone, but density is more sensitive to basalt fraction.

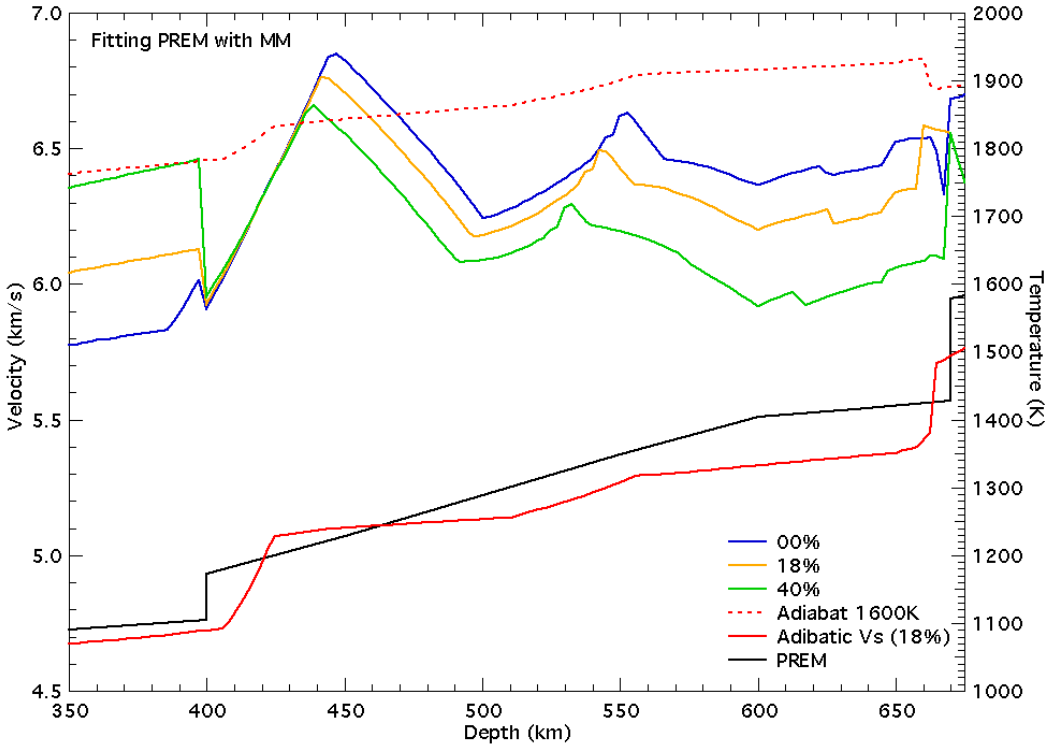

Figure 3.4 Same as figure 3.2 but using MM as the starting model. Colors indicate different basalt fractions as before. For the same basalt fraction EA and MM have identical bulk compositions.

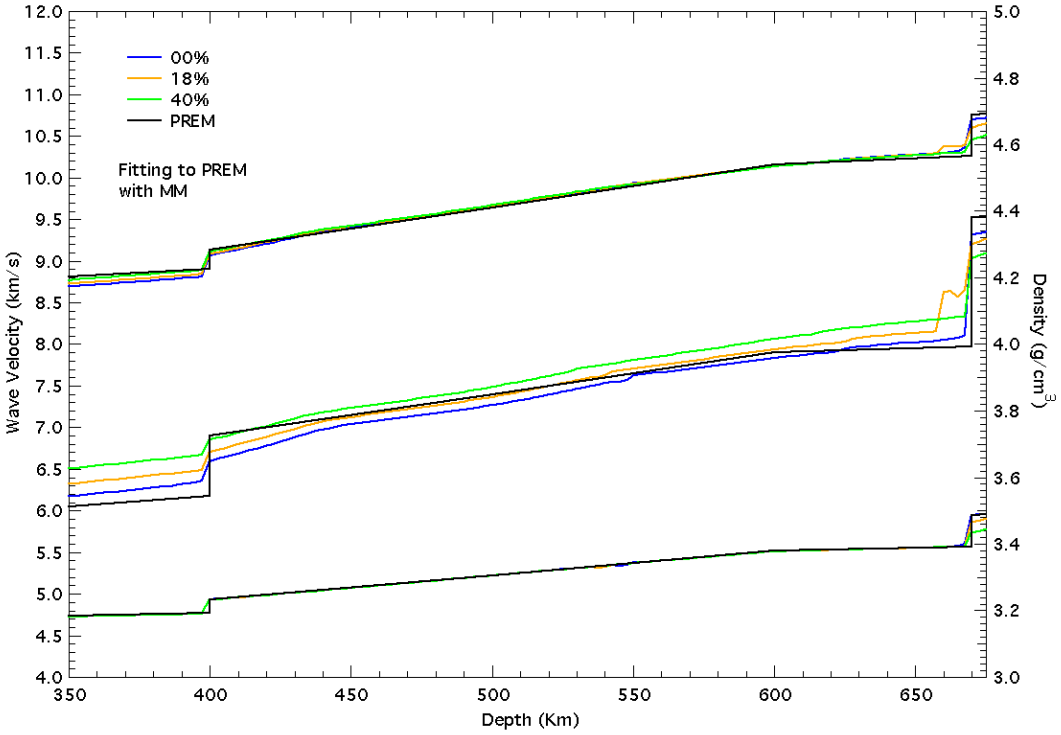

Figure 3.5. Lines as in figure 3.3. but for MM.

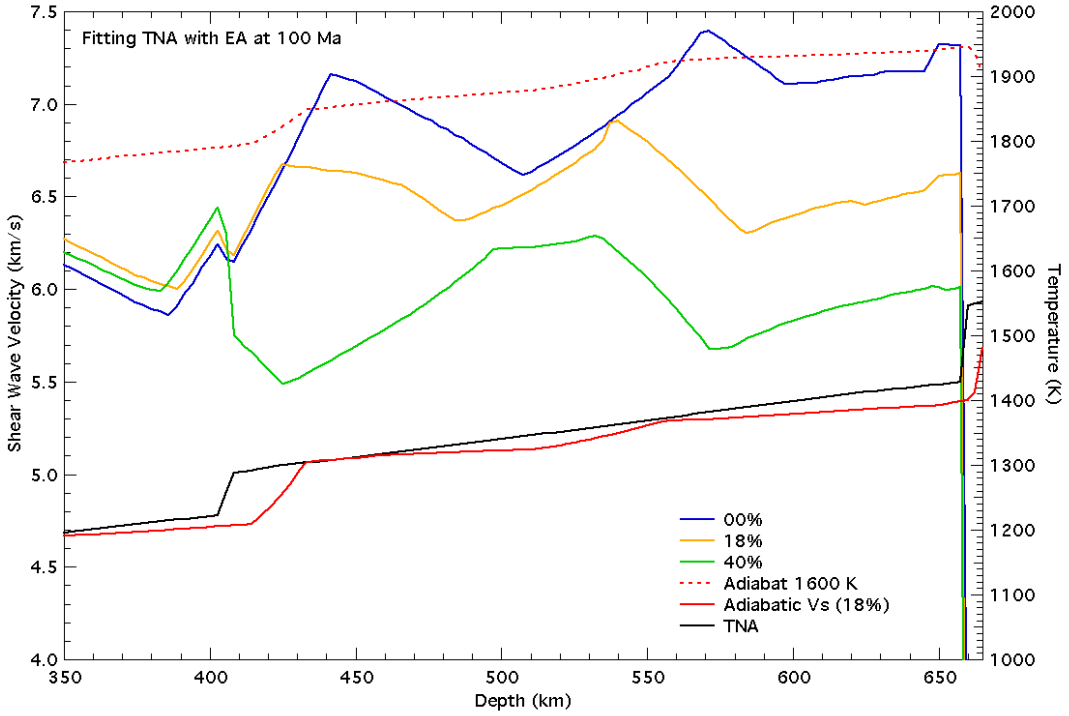

Figure 3.6 Fits to TNA starting from the EA compositional model and assuming 100 Ma geotherm. Results shown for basalt fractions of 0% (blue), 18% (orange), and 40%.

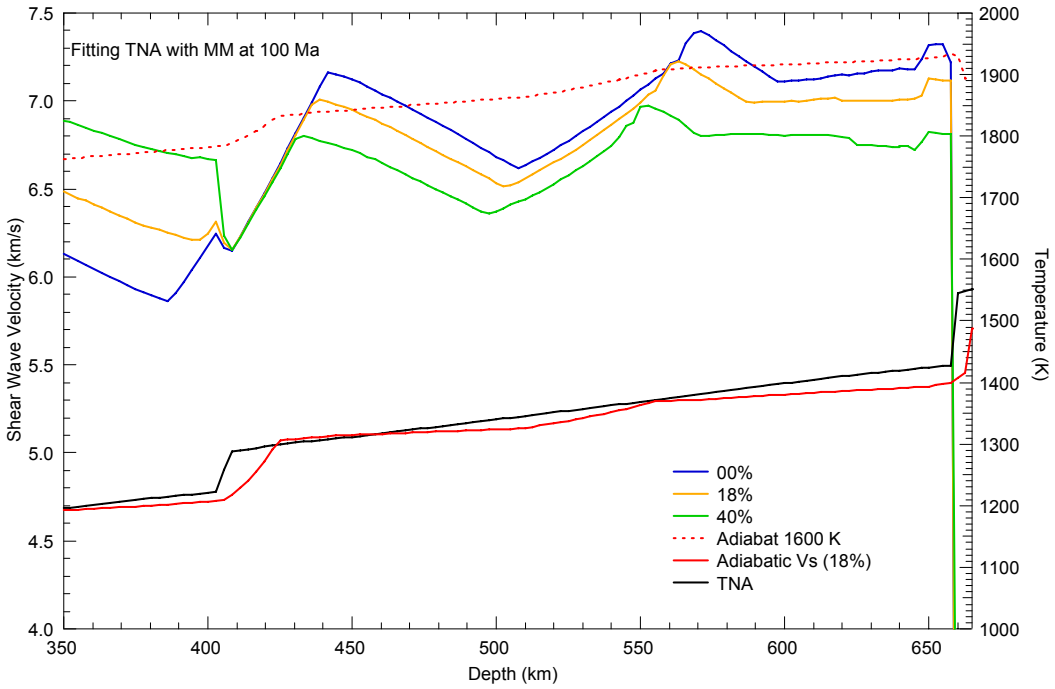

Figure 3.7 As in previous figure but using MM as the starting model. Note that starting from MM the deviations from adiabaticity are small.

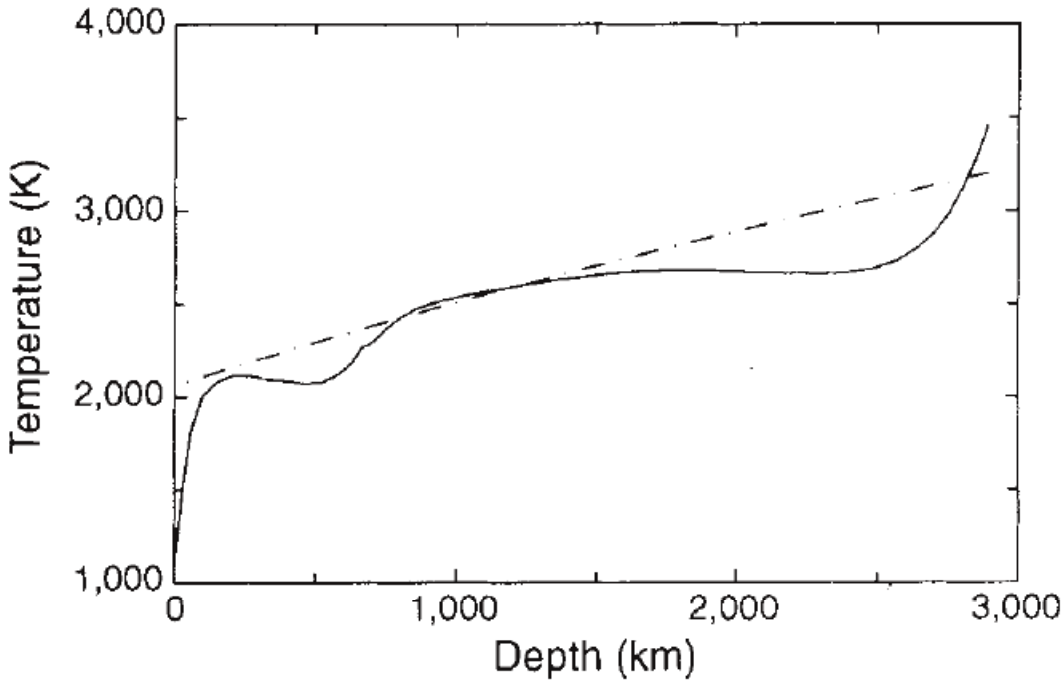

Figure 3.8. Solid line, radial profile of spherically averaged temperature for the last step of a global spherical computation of mantle convection in the presence of phase transitions. Dashed line is the reference state adiabat. From Tackley et al. (1993)

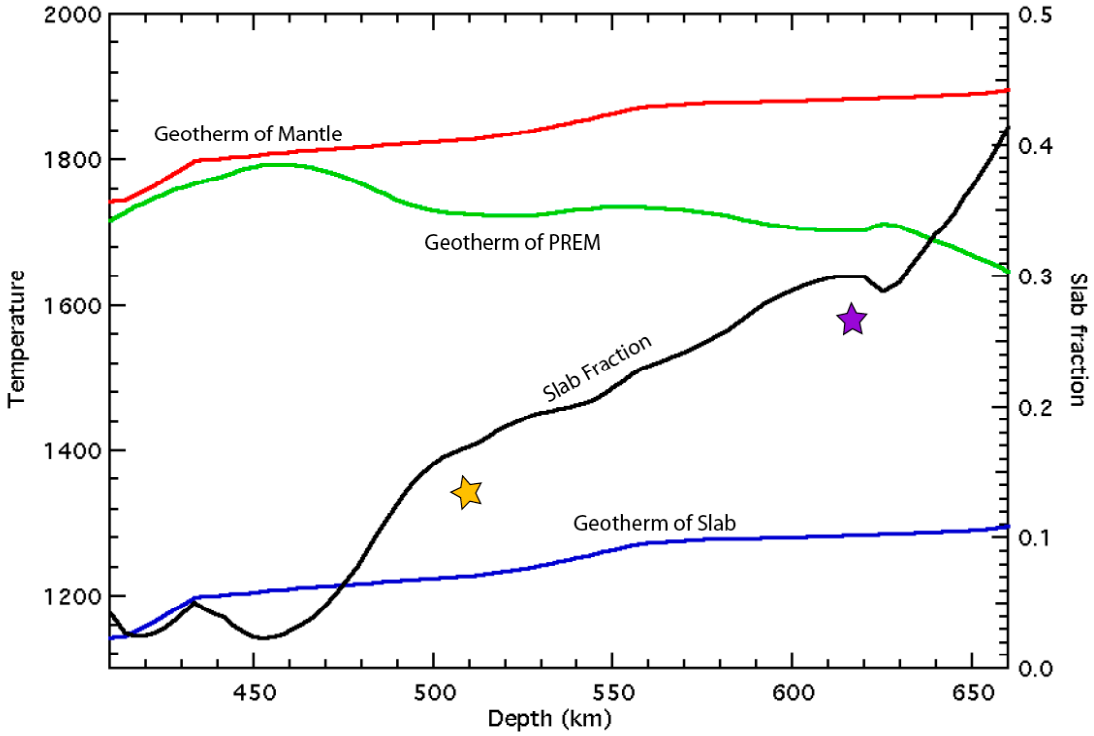

Figure 3.9, Slab accumulation in the transition zone. Red line is adiabatic geotherm of mantle with potential temperature 1550 K, green line is inverted geotherm of PREM model, blue line is geotherm of slab. Black line is slab fraction estimated by foumula $f_{slab}=(T_{mantle}-T_{PREM})/(T_{mantle}-T_{slab})$ in first order. Brown star is average slab mass fraction in the range of 435-570 km, and purple star is the average slab mass fraction in the range of 570-715 km, both of which are based on kinematic model by Lithgow-Bertelloni and Richards (1998)

a)

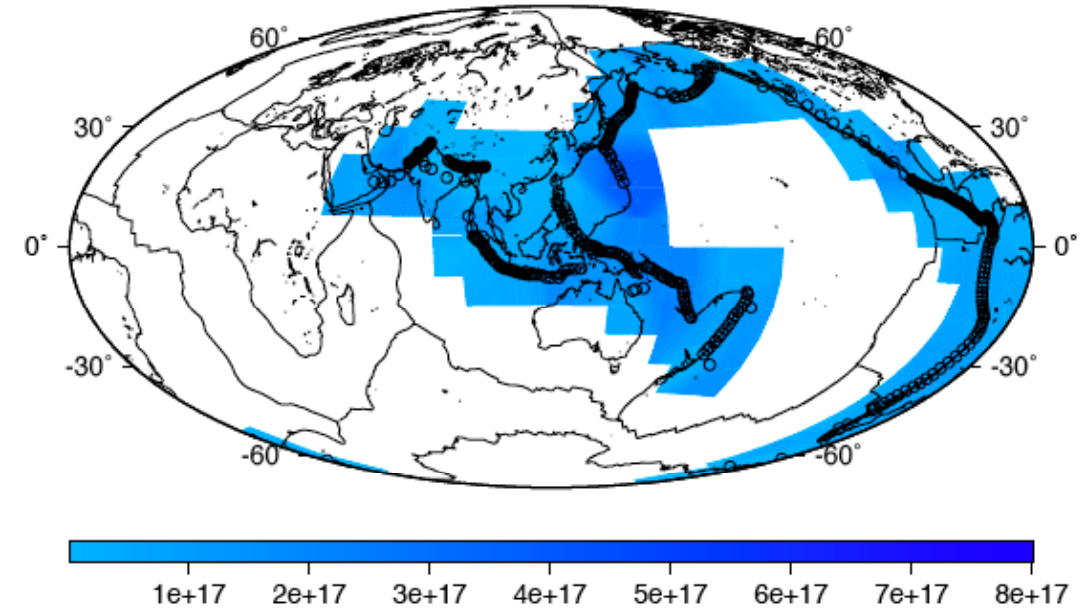

b)

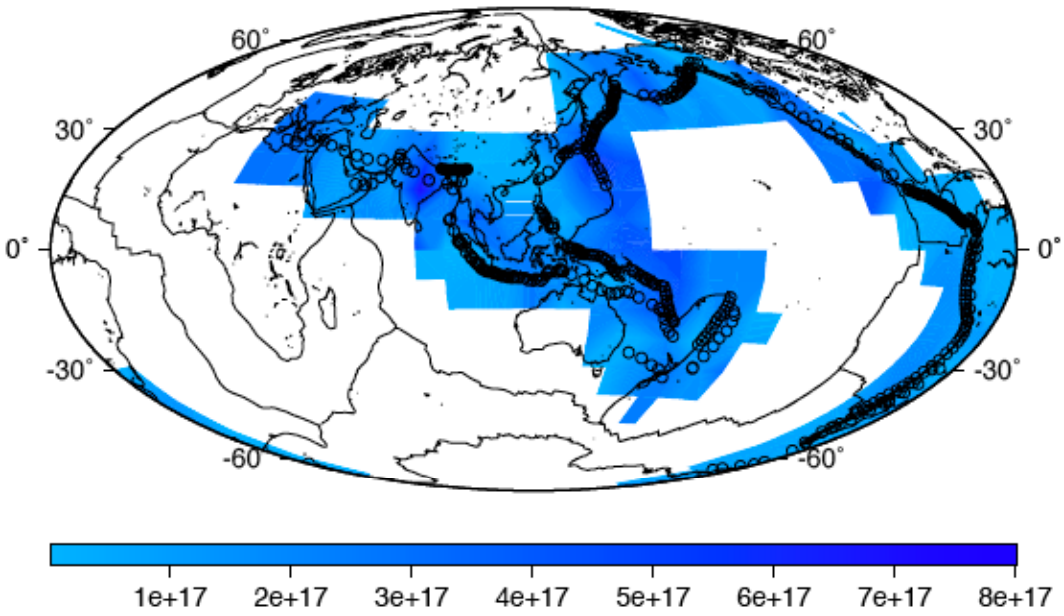

Figure 3.10 Kinematic model (Lithgow-Bertelloni and Richards, 1998) of where slabs may be in the transition zone based on 120 Myr of subduction and slabs are slowed down at 660 km depth due to an expected viscosity contrast between upper mantle and lower mantle. a) slab mass distribution in the depth of 435-570 km; b) slab mass distribution in the depth of 570-715 km.

3.5 Reference

Allegre, C.J., Brevart, O., Dupre, B., et al., 1980. Isotopic and chemical effects produced in a continuously differentiating convecting earth mantle. Phil. Trans. R. Soc. Lond. A 297,447-477

Allegre, C.J., Hofmann, A.W. and O'Nions, R.K., 1996. The argon constraints on mantle structure. Geophys. Res. Lett. 23,3555-3557

Anderson, D.L., 1981. Hot spos, basalts, and the evolution of the mantle, Science, 213, 82-89.

Bijwaard, H., Spakman, W. and Engdahl, E. R. 1998 Closing the gap between regional and global travel time tomography. J. Geophys. Res. 103, 30 055–30 078.

Bullen, K.E., 1963. An index of degree of chemical inhomogeneity in the Earth, Geophys. J. Int., 7, 584-592.

Bunge, H.P., Richards, M.A. and Baumgardner, J.R. , 1997. A sensitivity study of three dimensional spherical mantle convection at 108 Rayleigh number: Effects of depth dependent viscosity, heating mode, and an endothermic phase change, J. Geophys. Res., 102, 11,991-12,007.

Bunge, H.P., Ricard, Y., Matas, J. 2001. Non-adiabaticity in mantle convection, Geophys. Res. Lett., Volume 28, Issue 5, p. 879-882

Christensen, U., 1995. Effects of phase transitions on mantle convection. Annu. Rev. Earth plant. Sci. 23, 65-87

Davies, G.F.,1977. Whole mantle convection and plate tectonics, Geophys. J. R. Astron. Soc., 49, 459-486

Davies, G. F. 1988a. Ocean bathymetry and mantle convection. 1. Large-scale flow and hotspots. J. Geophys. Res. 93, 10 467–10 480.

Davies, G. F. 1988b. Ocean bathymetry and mantle convection. 2. Small-scale flow. J. Geophys. Res. 93, 10 481–10 488.

De Pallo, D.J. and Wasserburg, G.J., 1976. Nd isotopic variations and petrogenetic models. Geophys. Res. Lett. 3, 249-252

De Paolo, D.J., 1981. Nd isotopic studies: Some new perspective on earth structure and evolution, Eos Trans. AGU, 62, 137-140

Dziewonski, A. M., and Anderson, D. L. 1981. Preliminary reference earth model. Phys. Earth Planet. Inter., 25, 297-356.

Flanagan, M. P. and Shearer, P. M. 1998. Global mapping of topography on transtion zone velocity discontinuities by stacking SS precursors. J. Geophys. Res. 103, 2673–2692.

Fukao, Y., Obayashi, M. and Inoue, H. 1992 Subducting slabs stagnant in the mantle transition zone. J. Geophys. Res. 97, 4909–4822.

Fukao, Y., Widiyantoro, S. and Obayashi, M. 2001. Stagnant slabs in the upper and lower mantle transition region. Rev. Geophys. 39, 291–323.

Giardini, D. and Woodhouse, J. H. 1984. Deep seismicity and models of deformation in Tonga subduction zone. Nature 307, 505–509.

Grand, S.P., Helmberger, D.V. 1984. Upper Mantle shear Structure of North America. Geophys. J.R. astr. Soc. 76, 399-348

Grand, S. P. 1994. Mantle shear structure beneath the Americas and surrounding oceans. J. Geophys. Res. 99, 11 591–11 621.

Grand, S. P., van der Hilst, R. D. and Widiyantoro, S. 1997. High resolution global tomography: a snapshot of convection in the Earth. GSA Today 7, 1–7.

Hager, B. H. 1984. Subducted slabs and the geoid: constraints on mantle rheology and flow. J. Geophys. Res. 84, 6003–6015.

Heinz, D.L. and JEANLOZ, R., 1983. Inhomogeneity parameter of a homogeneous Earth, Nature 301, 138 – 139, doi:10.1038/301138a0

Honda S, Yuen DA, Balachandar S, Reuteler D. 1993. Three-dimensionalinstabilities of mantle convection with multiple phase transitions. Science 259:1308-11

Irifune T., Y. Higo, T. Inoue, Y. Kono, H. Ohfuji, K. Funakoshi, 2008. Sound velocities of majorite garnet and the composition of the mantle transition region, Nature, 451, 814-817.

Ito, E., and Katsura, T. 1989. A temperature profile of the mantle transition zone. Geophys. Res. Lett. 16, 425–428.

Jackson, I., Fitz Gerald, J.D., Faul, U.H., et al., 2002. Grain-size-sensitive seismic wave attenuation in polycrystalline olivine. J.Geophys. Res., Vol. 107, No. B12, 2360, doi:10.1029/2001JB001225

Jacobsen, S.B. and Wasserburg, G.J., 1979. The mean age of mantle and crustal reservoirs. J. Geophys. Res. 84, 7411-7427

K´arason, H. and van der Hilst, R. D. 2000. Constraints on mantle convection from seismic tomography. In The history and dynamics of global plate motion (ed. M. R. Richards, R. Gordon & R. D. van der Hilst), vol. 121, pp. 277–288. Washington, DC: American Geophysical Union.

Knopoff, L., 1964. The convection current hypothesis. Rev. geophys., 2, 59-123

Lithgow-Bertelloni, C. and Richards, M.A. 1998. The Dynamics of Cenozoic and Mesozoic plate motions.

Lundgren, P. R. and Giardini, D. 1994 Seismicity, shear-failure and modes of deformation in deep subduction zones. Phys. Earth Planet. Inter. 74, 63–74.

Machetel P, and Weber P. 1991. Intermittent layered convection in a model with an endothermic phase change at 670 km. Nature 350:55-57

Matyska, C. and Yuen, D.A., 2000. Profiles of the Bullen parameter from mantle convection modeling, Earth Plant. Sci. Lett., 178, 39-46.

Matyska, C. and Yuen, D.A. 2002. Bullen's parameter η: a link between seismology and geodynamical modelling Volume 198, Issues 3-4, pp 471-483

Nakagawa, T. and Buffett, B.A., 2004. Mass transport mechanism between the upper and lower mantle in numerical simulations of thermochemical mantle convection with multicomponent phase changes. Earth Plant. Sci. Lett., 230, 11-27

Nishimura, C.E., and Forsyth, D.W. 1989. The anisotropic structure of the upper mantle in the Pacific. Geophys. J. Int., 96, 203-229

O'Connell, R. J., 1977. On the scale of mantel convection, Tectonophysics, 38, 119-136.

Okino, K., Ando, M., Kaneshima, S. and Hirahara, K. 1989 A horizontally lying slab. Geophys. Res. Lett. 16, 1059–1063.

O'Nions, R.K., Evensen, N.M. and Hamilton, P.J. 1979. Geochemical modeling of mantle differentiation and crustal growth. J. Geophys. Res. 84, 6091-6101

Parmentier, E.M., Sotin, C. and Travis, B.J. 1994. Turbulent 3-D thermal convection in an infinite Prandtl number, volumetrically heated fluid: implications for mantle dynamics, Geophys. J. Int., 116, 241-251.

Peltier, W.R., 1976. Glacial-isostatic adjustment, II, The inverse problem, Geophys.J.R. Astron. Soc., 46, 669-705

Richards, M. A. and Wicks, C. W. J. 1990. S–P conversion from the transition zone beneath Tonga and the nature of the 670 km discontinuity. Geophys. J. Int. 101, 1–16.

Ringwood, A. E. and Irifune, T. 1988. Nature of the 650–km seismic discontinuity: implications for mantle dynamics and differentiation Nature 331, 131 - 136; doi:10.1038/331131a0.

Ritchter, F.M. and Johnson, C.E., 1974. Stability of a chemically layered mantle, J. Geophys. Res., 79, 1635-1639

Romanowicz, B., 1995. A global tomographic model of shear attenuation in the upper mantle. J. Geophys. Res. Vol. 100, No. B7, 12,375-12394

Schubert, G., Yuen, D.A., and Turcotte, D.L., 1975. Role of phase transitions in a dynamic mantle, Geophys. J. R. Astron. Soc., 42, 705-735

Schubert, G., 1979. Subsolidus convection in the mantles of terrestrial planets, Ann. Rev. Earth Planet. Sci., 7, 289-342

Solheim LP, and Peltier WR. 1994. Avalanche effects in phase transition modulated thermal convection: a model for the Earth's mantle. J. Geophys. Res. 99:6997-7018

Stixrude, L., Lithgow-Bertelloni, C., 2005a. Mineralogy and elasticity of oceanic upper mantle: Origin of the low velocity zone. J Geophys. Res. 110, B03204, doi:10.1029/2004JB002965

Stixrude, L., and Lithgow-Bertelloni, C., 2005b. Thermodynamics of mantle minerals – I. Physical properties. Geophys. J. Int., Volume 162 Issue 2 Page 610-632, doi:10.1111/j.1365-246X.2005.02642.x

Stixrude L., and C. Lithgow-Bertelloni, 2007. Influence of phase transformations on lateral heterogeneity and dynamics in Earth's mantle, Earth and Planetary Science Letters, , 263, 45-55.

Tackley PJ, Stevenson D J, Glatzmaier GA, et al., 1993. Effects of an endothermic phase transition at 670 km depth in a spherical model of convection in the Earth's mantle. Nature 361:699-704

Tackley, P. J., Stevenson, D. J., Glatzmayer, G. A., et al.,1994. Effects of multiple phase transitions in a three-dimensional spherical model of convection in Earth's mantle. J. Geophys. Res. 99, 15 877–15 901.

Tackley, P. J. 2000. Mantle convection and plate tectonics: toward an integrated physical and chemical theory. Science 288, 2002–2007.

Turekian, K.K. 1959. The terrestrial economy of helium and argon. Geochim. Cosmochim. Acta 17,37-43

Turner, G., 1989. The outgassing history of the Earth's astosphere. J.Geol. Soc. Lond. 146, 147-154

van der Hilst, R. D., Engdahl, R., Spakman, W., et al.,1991. Tomographic imaging of subducted lithosphere below northwest Pacific island arcs. Nature 353, 733–739.

van der Hilst, R. D., Widiyantoro, S. and Engdahl, E. R. 1997. Evidence for deep mantle circulation from global tomography. Nature 386, 578–584.

Wasserburg, G.J. and De Paolo, D.J., 1979. Models of earth structure inferred from neodymium and strontium isotopic abundances, Proc. Nal. Acad. Sci. U.S., 76, 3594-3598

Weinstein SA. 1993. Catastrophic overturn of the Earth's mantle driven by multiple phase changes and internal heat generation. Geophys. Res. Lett. 20:101-4

Xie, S. and Tackley, P.J. 2004. Evolution of helium and argon isotopes in a convecting mantle, Physics Earth Plant. Inter. 146, 417-439

Xu, W., Lithgow-Bertelloni, C., Stixrude, L., et al., 2008. The Effect of Bulk Composition and Temperature on Mantle Seismic Structure. Earth Plant. Sci Lett., Submitted

Zhou, H.W. and Clayton, R. W. 1990. P and S wave travel-time inversions for subducting slab under the island arcs of the northwest Pacific. J. Geophys. Res. 95, 6829–6854.